www.sciencemag.org/content/346/6208/458/suppl/DC1

Supplementary Material for

Medial prefrontal activity during delay period contributes to learning of a working memory task

Ding Liu, Xiaowei Gu, Jia Zhu, Xiaoxing Zhang, Zhe Han, Wenjun Yan, Qi Cheng, Jiang Hao, Hongmei Fan, Ruiqing Hou, Zhaoqin Chen, Yulei Chen, Chengyu T. Li*

*Corresponding author. E-mail: tonylicy@ion.ac.cn

Published 24 October 2014, *Science* **346**, 458 (2014)
DOI: 10.1126/science.1256573

This PDF file includes:

Materials and Methods
Figs. S1 to S35
Tables S1 to S8
Full Reference List

Other Supplementary Material for this manuscript includes the following:
(available at www.sciencemag.org/content/346/6208/458/suppl/DC1)

Movies S1 and S2

Materials and Methods:

Animals

Male adult C57BL/6 mice (SLAC, as wild type) or VGAT-Cre mice (*23*) were used for the current study (8-12 weeks of age, weighted between 20 to 30 g). Wild type mice were provided by the Shanghai Laboratory Animal Center (SLAC), CAS, Shanghai, China. VGAT-Cre mice were provided by Dr. H. Y. Zoghbi's group then bred in animal facility of the Institute of Neuroscience, Chinese Academy of Sciences. Mice were group-housed (4-6/cage) under a 12-h light-dark cycle (light on from 5 a.m. to 5 p.m.). Before behavioral training, mice were housed in stable conditions with food and water *ad libitum*. After the start of behavioral training, water supply was restricted. Mice could drink water only during and immediately after training. Care was taken to keep mice body weight (b.w.) above 80% of normal level. The behavioral and electrophysiological results reported here were collected from a total of 149 wild type mice and 103 VGAT-Cre mice. All animal studies and experimental procedures were approved by the Animal Care and Use Committee of the Institute of Neuroscience, Chinese Academy of Sciences, Shanghai, China.

Behavioral setups

We utilized an olfaction based delayed non-match to sample (DNMS) task in head-fixed mice, adapted from comparable behavioral paradigms in rats (*18, 19*). Computer controlled olfactometry systems were used for semi-automatic training (fig. S1). Microprocessor based controller was used to switch on/off the solenoid valves for controlling water and odor delivery in millisecond temporal resolution. Three-way solenoid valves were used for controlling air flow, whereas two-way solenoid valves were used for controlling water flow. Total length of odor-delivery tubes (inner diameter: 2.5 mm; outer diameter: 4.0 mm) was minimized to increase the turnover rate of odorants. An exhaust tube connected to a vacuum pump was used to further minimize residual odor and suck out the water not licked in time. Ethyl acetate (EA, boiling point 77.1°C) and 2-pentanone (2P, boiling point 101°C) were used at concentrations of 1:500 and 1:1000 (v/v in mineral oil, O122-4), respectively. We measured the concentration of odor by photoionization detector (PID). The readout of PID during the delay period was similar to that of the baseline level, indicating for efficient clearance of residual odor (fig. S6A). In hit trials water was provided at a speed of ~1.7 mL/min for half a second in a response time window. Multiple behavioral setups (early experiments with 6, later up to 20) were used. Each person can simultaneously handle up to six mice. Independent controller was used for each behavioral setup. Odor and water supply and the connection to vacuum pump were also independent for all behavioral setups. All facility parameters, including length for all tubes and air-flow rate, were kept the same across all behavioral setups. Behavioral results from 4~6 controllers were recorded simultaneously by custom written software and stored in computers.

Behavioral training

In DNMS task, a sample olfactory stimulus was presented at the start of a trial, followed by a delay-period (typically 4~5 sec) and then a testing stimulus, same to (matched) or different from (non-matched) the sample. Odor delivery duration was set to one second, which was sufficient for rodents to perceive olfactory cues (*31*). Mice were trained to lick in the response window in non-match trials. The response window (0.5 sec in duration) was started 1 sec after the offset of the second odor delivery. Licking events detected in the response window in non-match trials were regarded as *Hit* and will trigger instantaneous water delivery (0.5 sec in duration). *False choice* was defined as detection of licking events in the response window in match trials and mice were not punished in *False Choice* trials. Mice were neither punished nor rewarded for *Miss* (no-lick in a non-match trial) or *Correct rejection* (CR, no-lick in a match trial) trials. Licking events were detected by transistor-based licking-detectors (*32*) in optogenetic experiments and by infrared beam breakers in electrophysiological experiments. Odor and water delivery, laser illumination, and licking events were recorded by computers through serial ports. In each day, mice were required to perform 100 and 200 trials for optogenetic and electrophysiological experiments, respectively. Behavioral results were grouped in sessions of 20 trials for optogenetic and 40 trials for electrophysiological experiments, respectively. There was no break between sessions, i.e., session was used for convenience in presenting behavioral results. There was a fixed inter-trial interval of 10 sec between trials, unless stated otherwise. After training sessions ended each day, mice were supplied with free water until satiety.

Before the start of training, mice were water restricted for 1 to 2 days. The behavioral training process included habituation, shaping and DNMS learning phases. In habituation phase, mice were head-fixed in behavioral setups and trained to lick water from a water tube, encouraged with manually delivered water through syringes (5 mL). Tips of syringe needles (size of 27G) were cut and polished to ensure safety. Typically in 1 to 2 days, mice could learn to lick for 1 to 2 minutes without manual water delivery. The shaping phase was then started, in which only non-match trials were applied and water was provided in all 100 trials each day. In the beginning of shaping phase, water was delivered manually through syringes to encourage mice to lick in the response window. For every 10 to 20 trials, however, manual water delivery was temporally withheld to check whether mice could lick in the response window spontaneously. Shaping phase ended once mice could lick for water without manual delivery for consecutive 20 trials (one session). Typically the shaping phase lasted for 2 to 3 days.

The DNMS learning phase was then started from the next day, which was defined as Day 1 in the behavioral analysis reported in all figures. Both match and non-match trials were applied pseudo-randomly, i.e., two non-match and two match trials of balanced odor-pairs were presented randomly in every consecutive four trials. No human intervene was applied in DNMS learning phase to minimize any potential human bias in behavioral results. Typically behavioral performance was visualized in sessions (Fig. 1C). The performance correct rate (referred to as “performance” in labels of figures) of each session was defined by:

Performance correct rate = (num. hit trials + num. correct rejection trials) / total number of trials

Hit, *False choice*, and *Correct rejection rates* were defined as follows:

Hit rate = num. hit trials / (num. hit trials + num. miss trials)
False choice rate = num. false choice trials / (num. false choice trials + num. correct rejection trials)
Correct rejection rate = num. correct rejection trials/ (num. false choice trials + num. correct rejection trials)

Discriminability (*d'*, (*33*)) was also used to quantify performance, as defined by:

d'=norminv(Hit rate)- norminv (False choice rate),

in which *norminv* was the inverse of the cumulative normal function. Conversion of *Hit* or *False choice* rate was applied to avoid plus or minus infinity (*33*). In conversion, if *Hit* or *False choice* rate was equal to 100%, it was set to [1-1/(2*n*)]. Here, *n* equaled to number of non-match or match trials, respectively. If *Hit* or *False choice* rate was zero, *it* was set to 1/(2*n*).

In fig. 18C, the Δ performance, Δ hit and Δ correct rates for each mice group were defined as the values of laser-on trials minus that of laser-off trials.

Licking efficiency was calculated as:

Licking efficiency = rewarded licking number / (*rewarded licking number + unrewarded licking number*)

The '*rewarded licking number'* referred to the number of licking events in a 2.5 sec time window, after the onset of the second odor delivery, in non-match trials (rewarded trials). The '*unrewarded licking number'* referred to the number of licking events in the same time window in match trials (unrewarded trials).

In the DNMS experiments with varied duration in the delay period, the mice firstly received initial training with the delay period of 5 seconds. After the mice were well-trained, they were exposed with the delay period of different durations in one day. Therefore, the training history for the delay periods of 8, 11, 14, 17 sec was the same, when the mice exhibited decline of performance with increasing duration of the delay period (fig. S4B).

In the four-odor DNMS task (fig. S4C), ethyl acetate, 2-pentanone, methyl butyrate, and ethyl propionate were used for match or non-match odor pairs. Mice were firstly well-trained with DNMS task of two odorants and then tested with four-odor DNMS task.

For the optogenetic experiments with the blind design (Fig. 2A-2D, Fig. 3A-3F, fig. S7, S9-S14, S16-S19, S21, S22), R.Q. Hou labeled containers for viruses with "A", "B", etc. before injection. She would not participate in behavioral and optogenetic experiments or data analysis. Care was taken to ensure that the true identities of the viruses were unknown to the experimenters performing behavioral and optogenetic experiments. R.Q. Hou would not reveal the identity of viruses, until all the analysis of the behavioral and optogenetic experiments had been finished and results plotted.

In the non-match to long duration sample (NMLS) experiments that measured the delay-period residual threshold for DNMS (fig. 6B, 6C), three sets of odor delivery were applied sequentially in each trial. The first delivery of odorant (butyl formate, 1 sec in duration) provided the trial starting signal without correlation with behavioral outcomes. The second set of odor (4 sec in duration) was designed as the odor sample, which was either ethyl acetate or 2-pentanone. Immediately following the sample, the third set of odor (1 sec in duration) was delivered, matched or non-matched to the sample. Mice were rewarded with water if they licked in the response window in non-match trials. The concentration of the sample odorant was systematically varied to measure the concentration threshold of chance level performance in NMLS.

In the non-match to sample without delay period (NMS-WD, Fig. 3C, 3D) experiments, mice were trained to perform NMS task, in which sample odor delivery and testing odor delivery was separated only with 200 ms interval. Four independent odor bottles were used for odor delivery in NMS-WD experiments. Shaping sessions in NMS-WD were similar to DNMS task, only without the delay period.

In the Go/No-go (GNG) experiments, mice were trained to lick for water after the GNG cues of ethyl propionate (Go) and methyl butyrate (No-go). In the shaping sessions of the GNG task, water was delivered after both ethyl propionate and methyl butyrate. The GNG task in main text (Fig. 3E, 3F) was termed as GNG-ri, because that the inter-trial interval was random (in 6-10 sec range) and a trial-starting cue (propyl formate) was present before GNG cues (5 sec before the onset of Go/No-go cue). In the Fig. S20 of the Supplementary Material, the GNG task was termed as GNG-fi task, which had a fixed inter-trial interval (10 sec) and there was no trial-starting cue. By adding trial-starting cue and random inter-trial interval in GNG-ri task, the period of laser illumination in GNG task became behaviorally more relevant, because in this manner the period following trial-starting cue became predictive for the upcoming decision making cue. Mice need increased number of trial to reach the criterion (performance reaching 80% in successive 20 trials) in learning the new GNG task, as compared to the previous GNG task (132 ± 6 for the new design, 68 ± 10 for the original design, Mean ± SEM, $p = 0.0013$, Mann-Whitney U-test, Fig. S20B), suggesting a potential effect of the added requirement for sustained attention.

In the results included with well-trained phase of optogenetic experiments, mice were initially trained under a fixed number of trials (100 trials, or 5 sessions) each day of learning phase (Day 1-5). Then in Day 6 and 7, behavioral training was continued until mice were satiated (5-15 sessions per day); no optogenetic manipulation was applied in these two days. In Day 8, the protocol of a fixed number of trials (100 trials) was resumed.

Virus preparation

The vector of DDREAD experiments was provided by Dr. B.L. Roth (*22*). Other vectors were obtained from AddGene, US. Packages of AAV2/8 viruses were provided by Neuron Biotech, Shanghai, China. Viral titers were 4×10^{12} particles / mL for AAV-EF1α-DIO-mCherry, 4×10^{12} particles / mL for AAV-EF1α-DIO-hChR2-mCherry, 7×10^{12} particles / mL for AAV-CaMKIIα-hChR2(H134R)-EYFP, 2×10^{13} particles / mL for AAV-CaMKIIα-EYFP, 9×10^{12} particles / mL for AAV-CaMKIIα-mCherry, 7

$\times 10^{12}$ particles / mL for AAV-CaMKIIα-eNpHR3.0-EYFP, 1.32 x 10^{13} particles / mL for AAV-hSyn-HA-hM4D (Gi) -mCritrine.

DDREAD experiment

Clozapine-N-Oxide (CNO) was dissolved in Dimethyl sulfoxide (DMSO, D2650, Sigma) to a stocking solution of 0.4g/mL and diluted with saline (0.9% NaCl solution) to a working concentration of 0.2 mg/mL. Stocking solution was stored at 4℃ and fresh CNO solution was prepared each day before experiments. Saline or CNO (1 mg/kg b.w.) was administered intraperitoneal (i.p.) to the mice 40 min before behavioral testing or extracellular recording *in vivo* (Fig. 1E), in the blind design similar to that of optogenetic experiments.

Stereotaxic virus injection and optical fiber implantation

Mice were anaesthetized with analgesics (Sodium pentobarbital, 10mg/mL, 120 mg/kg b.w.) before surgery. All surgery tools, materials, and experimenter-coats were sterilized by autoclaving. Surgery area and materials that cannot undergo autoclaving were sterilized by ultraviolet radiation for more than 20 minutes. Aseptic procedures were applied during surgery. Anesthetized mice were kept on a heat mat to maintain normal body temperature. Scalp, periosteum, and other associated soft tissue over skull were removed. Skull was cleaned by 3% hydrogen peroxide solution and then by filtered artificial cerebrospinal fluid (ACSF) with cotton applicators. After skull was dried out, a layer of tissue adhesive (as in (*34*)) was applied on surface of skull. A steel plate was placed on skull and then fixed by dental cement, without blocking intended injection area. Craniotomies of ~1 mm in diameter were made bilaterally above mPFC. An injecting pipette was pulled from a glass tube (Borosilicate glass with filament) to a sharp taper. The tip of a pipette was grinded to 7~8 μm in diameter with 45° grinding angle by a micro-grinder. A pipette was installed into a holder and connected with a vacuum pump. It was then lowered into a virus container till the tip immersed in virus solution. About 0.5 μL virus was loaded with a negative pressure of ~14 mm Hg. A picosprizer pump was then used to apply pressure of 6-14 psi to pipette for virus injection. A stimulator was used to feed TTL pulses to trigger the picosprizer. The parameters of TTL pulses were 0.1s in duration and 1 Hz in frequency. Virus (0.5 μL in volume) was delivered to each hemisphere at AP 1.96 mm, ML 0.42 mm, DV 1.62 mm targeting for prelimbic area (PL), a part of mPFC. For hM4Di experiment, virus (0.4μL in volume for each site) was injected to two sites in each hemisphere, with coordinates of AP 2.2 mm, ML 0.25 mm, DV 1.0 mm and AP 1.87mm, ML 0.75, DV 1.5mm. After each injection, the pipette was left in tissue for 10 minutes before slowly withdrawn, to prevent virus spilling over. Two optic fibers (200 μm in diameter, 0.37 NA, 3mm in length) with ceramic ferrule were implanted with an angle of 26º. Tips of optical fibers were 300 μm over the virus injection sites in mPFC for each hemisphere, with the coordinates of AP 1.96 mm, ML 0.55 mm, DV 1.35 mm. For virus injection in S1, coordinate of virus injection sites was bilateral AP -1 mm, ML 3.5 mm, DV 0.4 mm (from dura). The tips of optical fibers were 300 μm over the virus injection sites in S1 for each hemisphere, with the coordinates of AP -1 mm, ML 3.5 mm, DV: 0 mm (onto the dura). A thin layer of tissue gel (Kwik-Sil, silicone elastomer, only single component was used) was used to prevent contact of dental acrylic to brain tissue. Dental acrylic and cement were mixed and applied to connect skull, plate, and optical fibers for structural support. Mice

were recovered under a heat lamp or on a heating pad after surgery. Antibiotic drug (Ampicillin sodium, 20 mg/mL, 160 mg/kg b.w.) was i.p. injected each day for the following three consecutive days.

Laser illumination designs in optogenetic experiments

In optogenetic experiments, an external optical fiber (200 μm in diameter, NA: 0.37) was coupled to an implanted optic fiber through a ceramic sleeve. Laser power at the end of an external fiber was measured with a laser power meter and was adjusted to meet experimental requirement. Laser illumination was provided with blue (473 nm) or green (532 nm) diode pumped solid state laser (50 mW) and controlled by a microcontroller. For experiments with ChR2 in GABAergic neurons (e.g. Fig. 2A, 2B, 2E, 2F, Fig. 3C-3F), laser power was 2 mW at tips of fibers in brain tissue. For those with ChR2 in excitatory neurons (e.g. Fig. 3A, 3B), laser power was 0.8 mW. For NpHR experiments (e.g. Fig. 2C, 2D), laser power was 10 mW. For optogenetic experiments, laser illumination was provided in learning phase (Day 1-5) and then stop till mice reached well-trained criterion (>90% performance correct rate in one day, usually ≥ Day 8). Laser illumination was then applied again to obtain results for well-trained phase.

The current study utilized two designs for laser illumination: laser on in all trials and interleaved laser on/off design. The first design was meant to exert maximal optogenetic effect, which can be compared across groups of mice with different viruses expressed. This design maximally utilized the advantage of blind design that we used. The second design was meant to study the potential trial-by-trial effects of optogenetic manipulation to behavioral performance, which can reveal whether optogenetic manipulation specifically influence the laser on trials instead of general influence of performance across all trials. It also better controls for variation across individual mice.

Verification of optogenetics

All recordings were conducted in awake head-fixed mice with implanted op-tetrodes. For five VGAT-Cre mice expressing AAV-DIO-ChR2 virus, constant illumination of blue laser (473 nm, 2 mW) reliably suppressed neural activities in 80 out of 102 recorded neurons (Fig. 2B). For the two wild type mice expressing AAV-CaMKIIα-eNpHR3.0, activities of all 19 neurons were suppressed by constant green laser illumination (532 nm, 10 mW; Fig. 2D). Thus the methods were effective in suppressing activities of pyramidal neurons. For the wild-type mouse expressing AAV-CaMKIIα-ChR2, laser illumination (473 nm, 2 mW, 8 Hz) induced reliable excitation in 129 out of 145 recorded neurons (Fig. 3B). Other 16 out of 145 recorded cells in the CaMKIIa-ChR2 experiments showed a suppression of activity during laser illumination, which should be due to the feedback inhibition of local circuit. On average the method was effective in enhancing activities of pyramidal neurons ($p < 0.05$, Mann-Whitney U-test). We are uncertain of the relative advantage of the methods between indirect suppression by activating VGAT-Cre neurons and direct suppression with NpHR, besides the fact that there appeared to have less rebound excitation with ChR2 expression in GABAergic neurons (comparing firing rate modulation in Fig. 2B and 2D).

Immunostaining and imaging experiments

Mice were deeply anesthetized with sodium pentobarbital (120 mg/kg) and then perfused transcardially with 20 mL saline followed by 20 mL paraformaldehyde (PFA, 4%, w/v) in PBS. The brains were removed and kept in 4% PFA at 4℃ overnight, then transferred to PBS. Coronal slices (50-80 μm in thickness) were obtained using a vibratome and collected in PBS. For GABA immunostaining, slices from VGAT-Cre mice injected with AAV-DIO-ChR2-mCherry were incubated with blocking solution (5% Bovine serum albumin, w/v in PBS, mixed with 0.5%Triton X-100, v/v) at 4℃ overnight and then with diluted primary antibody (A2052, Sigma, 1:1000) in 3% Bovine serum albumin in PBS with 0.3% Triton X-100 at 4℃ overnight. After washing three times with PBS (10 min each time), slices were incubated with florescent second antibody (A21206, Alexa 488, Invitrogen, 1:1000) for 2 hours at room temperature. Slices were then washed with PBS (once, 10 min) and incubated with DAPI (C1002, Beyotime, 1:1000 diluted in PBS) for 10-15min. After three times of washing by PBS (10 min each time), slices were mounted and coverslipped. For experiments without requirement of GABA staining, slices were directly incubated with DAPI and then mounted and coverslipped. Fluorescence images were then obtained with a confocal microscope and 10X (0.45 NA) or 20X (0.75 NA) objective lens. Images were analyzed with ImageJ (NIH, US).

Generation of overlaid histology maps for all mice

The overlaid histology images for immune-staining figure showed in fig. S7, S12, S17 was plotted in the following steps:
Six coronal brain sections (Bregma +2.58, 2.34, 2.1, 1.98, 1.78 and 1.54 mm, adapted from the atlas of Paxinos & Franklin 2008) were selected as example positions to present virus targeting regions from those mice used in optogenetic manipulation experiments. For each mouse with same virus expressed, viral expression areas on these selected brain slices were traced out to obtain area of interests. Areas outside of the area of interests were set as 0 and interested areas as 1 to generate 0-1 matrix figures for each brain slice. These matrix figures from different mice (number: n) were then summed to generate a overlaid image with number from zero to n. Darkness (gray scale) of this summed matrix figure was used to generate the overlaid histology map for a given group. Darker the pixel, higher the number of mice had expressed intended molecules. We then repeated the above procedures for all groups of brain slices with different viruses expressed.

Assembly of chamber for microdrive

Tetrode-microdrives used for chronic recording were home-made adapted from methods in (*35-39*). The method to assemble a microdrive chamber was modified from (*38*). A chamber of a microdrive was composed of eight pieces of printed circuit boards (PCB) (0.05 mm thickness, fig. S23A), which were designed with Altium Designer and manufactured in Binqidianzi, Shanghai, China. Parts 1 and 2 were stacked and glued together to form the ceiling of a microdrive. Holes (Pt. 1b, 1c and Pt. 2b, 2c) on the ceiling were for holding the larger end (Pt. 7a) of screws Pt. 7 (11 mm in length and 2.0 mm in diameter). Parts 3 and 4 were stacked and glued together to form the floor of a microdrive. Two smaller

holes (Pt. 3b, 3c) on the floor were for restricting the smaller end (Pt. 7b) of screws (Pt. 7). Other sets of smaller holes ('d' and 'e' in Pt. 2-4) were used to hold two metal rods (Pt. 8), which was designed to prevent nuts (Pt. 7c) from rotating while turning screw head (Pt. 7a). This design transferred rotation of screw heads into movement of nuts through screw axis, therefore drove tetrodes (glued to nuts Pt. 7c) into brain tissue. Each microdrive had two independently movable screws (Pt. 7) and corresponding nuts (Pt. 7c). Two pieces of PCBs (Pt. 6) were glued to be side plates of the chamber (9 × 9 × 12 mm).

Assembly of tetrodes or op-tetrodes

The method for tetrode assembly was modified from (*38, 39*) and shown in fig. S23B. Each tetrode was constructed with polyimide insulated, Ni-Chrome wire (12.5 μm core diameter for tetrode). Construction of a tetrode was started by obtaining a 20 cm long wire. Wire was folded in half for twice, and then its open end was clamped together with a clip. The 'a' end of wires (fig. S23B) was hanged onto a horizontal bar. A rotating force was applied to the clip manually to trigger counter-clock wise twists. After the counterclockwise twisting stopped, freely clockwise unwinding was allowed until the clip stopped rotating. After tetrode twisting was completed, insulation coats of wires were melted and fused together by gently heating with a heat gun (200° C) for 4-5 sec. Tetrode was removed from the twisting apparatus by gently lifting the clip and cutting the wire near the clip. The clip was gently lifted and the tetrode wire was cut near the clip. Tetrode then was removed from the twisting apparatus. At the 'a' end of wires, the loop was cut into four non-bonded strands of equal length. Individual strands were separated by gently bending wires with a soft tipped tweezer. Insulation coats of strand tips were removed carefully. Then wire tips were soldered to corresponding pins on a PCB connector which was electrically connected to an adaptor. Two electrodes for ground and reference (magnet wire, 0.01 mm^2) were soldered to the corresponding pins. Each pin was individually coated with silver paint to enhance conductance. Connector pin arrays and Omnetics adaptors were then coated with silica gel to protect connection between wires and pins

Assembly of microdrive

The final assembly steps were shown in fig. S23C. Pieces of polyimide tubing (inner diameter 75 μm, outer diameter 150 μm) were glued together (2 × 4) to form guide tubes. They were then inserted and glued on the wall of lower holes ('f' and 'g' in Pt. 3-4, shown in fig. S23A). Tetrode wires were inserted into guide tubes from the side of a micro-drive chamber. Then with epoxy glue (5 min epoxy system), middle part of tetrode wires were fixed on each of two independently movable screw nuts (Pt. 7c) in a microdrive chamber. After epoxy glue dried, electrode end of tetrodes were trimmed and the length out of guide tubes was adjusted. Trimmed tips of tetrodes were electroplated to a final impedance of about 1MΩ at 1kHz, with an automatic multichannel electroplating system. In electroplating, low concentration of gold solution was prepared by mixing with solution of polyethylene glycol (PEG, 1mg/mL, v/v) at a concentration of 1:9 (Gold : PEG). Omnetics adaptors were then fixed on side plates (Pt. 6) of a microdrive chamber.

For assembly of op-tetrodes, extra guide tubes (inner diameter 250 μm， outer diameter 350 μm) were added for optical fibers. One or two optical fibers were inserted into a microdrive chamber through the guide tubes. Epoxy and silica gel were applied sequentially to secure stability of optical fibers. To reduce electrical noise, a microdrive chamber was gently wrapped with a thin layer of copper foil, which was electrically connected with ground wire. Each microdrive was composed of 16 tetrodes with 8 for each hemisphere.

Surgical implantation of tetrode/op-tetrode microdrive

The implantation procedure was similar to that for implantation of optical fibers. A microdrive was sterilized by ultraviolet radiation for more than 20 minutes. Two cranial windows of 2 by 1 mm were made in each hemisphere for implantation. The center of an electrode array was targeted to AP +2 mm, ML 0.4 mm, and DV 1.65 mm for PL. Dura mater was carefully removed with surgery needles with as less bleeding as possible. Similar to optical fiber implantation, tissue gel (3M, US) and dental cement were carefully applied without relative motion between a microdrive and brain tissue. Antibiotic drug (ampicillin sodium, 20 mg/mL, 160 mg/kg b.w.) was injected for three consecutive days after surgery.

Electrophysiological Recording

After surgery, mice were allowed to recover for at least one week before behavioral training. The recording began after the end of shaping period. We did not select cells to be recorded to ensure independent sampling. In experiments of daily lowering electrodes (Fig. 4; fig. S30-S35), wide band signals (0.5-8000 Hz) from all tetrodes were amplified (× 20000) and digitized at 40 kHz with the Multineuron Acquisition Processor and all data were saved to a hard-disk. Spike event detection and sorting was performed offline as described below. Recording tetrodes were lowered for ~60 μm each day by turning the screw (Pt. 7a) for about 90 degree. For results without daily lowering of electrodes (fig. S25-28), tetrodes were not lowered each day. Raw signal was filtered online (250 - 8000 Hz) and only spikes detected across threshold (6 folds of STD) were stored for further analysis.

Acute recording were performed on C57 mice with AAV- CaMKIIα-ChR2-mcherry virus injected to mPFC 3 weeks before surgery. On the day before recording, optical fibers were implanted with the same procedure and to same location as previously described. Before recording, mice were anesthetized by isoflurane and dental cement and skull above PFC was removed. After fully awaken from anesthetization, mice were headfixed and silicon probes (NeuroNexus) were inserted with different lateral distance from the optical fiber to detect the range of neural activations. Constant illumination of blue laser (473 nm, 2 mW) reliably enhanced neural activities in 129 out of 145 recorded neurons (laser period having significantly higher firing rate than baseline period, Mann-Whitney Test, $p<0.05$, Fig. 3B).

Analysis: Spike sorting

Spike sorting was performed adapted from ref (*40, 41*). Care was taken to ensure that only single-units

were sorted and analyzed, based on clustering analysis on principal components (PC) of spike waveforms. Offline spike detection was performed with OfflineSorter. Raw signals were filtered in 250~8000 Hz to remove field potentials. Typically negative six times of standard deviation of recorded signals of each lid of a tetrode were set as thresholds for detecting spike events. Deflections lower than the threshold were marked as putative spike events. Spike events that were detected at any lead of a tetrode would retrieve corresponding waveforms at all four lead for further analysis. PCA was performed for tetrode-waveforms to extract the first three PCs explaining the largest variance. Then, "T-Dist EM" clustering provided by OfflineSorter was performed in 3D PC space of waveforms. Single neuron was included only if there were no more than 0.1% of spikes within 2 ms refractory period and the averaged firing rate was higher than 2 Hz. Recording stability was verified by visually inspection of PCs projection of spike waveforms throughout recording. To ensure genuine single-units, we plotted and inspected spike amplitudes and peak-to-valley intervals of recorded spikes. In this plot, multiple clusters meant multiple neurons or a noise source were included. A sharp cut-off in either side of distribution meant significant missed spike events. We therefore excluded the units from the further analysis in either of above cases. Including them in the analysis, however, did not affect the results in learning specific modulation in delay-period activities, PCA trajectories, decoding, and correlation with behavioral performance (data not shown). To guarantee independent sampling of neurons across different days, we compared spike waveforms and autocorrelation to detect putative same neurons recorded in different days. For those neurons, only the activity of the first recorded day was included. Each day we can record 2 to 13 single-units (median 8) from one mouse. The unsorted spike events were analyzed as multi-units, with similar conclusion with single-unit (data not shown).

Analysis: Spike count and activity heat map

All further analyses were performed by custom-written codes with MATLAB. Statistical significance was defined as $p < 0.05$ unless noted otherwise. Baseline period was defined as two seconds before onset of odor sample. Firing rate from each trial of baseline was averaged to form baseline activity vector of each neurons. Mean and standard deviation of this baseline activity vector were used to convert averaged firing rate of different time bins (size: 100 ms) into Z-score. Activity of all neurons were sorted by the mean Z-scored firing rate and plotted as heat map using 'Jet' color-map defined in Matlab (Fig. 4D, fig. S26). To quantify the difference of modulation in delay firing in learning and well-trained phases, we separated the cells into enhanced and suppressed groups, by signs of averaged activity in delay-period compared to that in baseline (Fig. 4E).

Analysis: Population trajectories

We adapted the procedures of (*25, 42*) to retrieve population trajectories (Fig. 4F, 4G, fig. S27, S30-S32). Averaged firing rate of each mPFC neuron for particular odor sample defined one dimension in an abstract space of population activity profiles. Neurons recorded from different mice in a same training day were grouped together to generate high dimensional neural firing patterns representative for different stages of learning in the WM task. To visualize this high dimensional data, we performed PCA and projected firing dynamics onto the first three PCs, which are eigenvectors with the largest eigenvalues of covariance matrix of the original firing patterns. In calculation of PCA, equal number of

neurons (ninety) was randomly selected for each day in learning and for well-trained phase. This procedure reduced dimensionality while still retaining the maximum variance (*25, 42*). In our study the first three PCs represented 72 ± 5% of variance (mean ± SEM, n = 6, for different days through training process). Binned firing rates (bin size: 200 ms) for all neurons in each training day were used as inputs for PCA. The resulting first three PCs explaining the largest variance were used to generate trajectories shown in Fig. 4F. To calculate the population trajectory distance evoked by different first odor, we used the first 20 PCs (representing over 80% variance). The Euclidian distance of the trajectories of these 20 PCs was calculated for each time bin. To visually inspect the internal noise of the PCA distance, for each run of the distance analysis, trials started with odor samples (EA and 2P) were randomly separated evenly as EA1, EA2 and 2P1, 2P2 groups. The averaged firing rates for each group were used to calculate PCA and generate distance between different odor (e.g. EA1 to 2P1) and within same odor (e.g. EA1 to EA2). The same procedure was repeated for 100 times. Normalized distance was averaged and then plotted to generate Fig. 4G. Confidence interval of 95% was used to calculate statistical significance from baseline.

Analysis: Decoding

We modified the procedure of (*26*) to perform the decoding analysis (fig. S33, S34):

1) Difference in the number of neurons recorded each day may bias decoding efficiency. To allow a fair comparison, we randomly selected 90 neurons recorded each day for decoding analysis.
2) We randomly selected 160 trials for each unit (80 for EA and 80 for 2P as the first odorant). The duration of the whole trial was 17.6 sec. The bin size for calculating the firing rate was 200 ms and 138 bins were created for each trial. The resulted population activity matrix had the dimension of 90 × 160 × 138.
3) For each first odorant, the activity template was created by averaging firing rate from half of the trials (40 randomly selected out of 80) for all the neurons. The resulting template had the dimension of 90 × 138.
4) One testing trial for a given first odor was randomly selected from the 40 remaining trials not included in template calculation, resulting in a testing matrix with the dimension of 90 × 138.
5) For each time point of 138 bins, we separately calculated the correlation coefficients between the testing vector and each of the two template vectors, all with dimension of 90 × 1.
6) The testing vector was assigned as decoded odor A or B according the larger correlation coefficient with the corresponding template vector. The truth score of 1 or 0 was assigned if the assignment was correct or not, respectively.
7) The same procedure from 5th to 6th was repeated for all the time bins, to generate a truth score vector (with the dimension of 1 × 138).
8) The procedure from 5th to 7th was repeated five times. The resulting 5 × 138 matrix was averaged to obtain a classification accuracy vector (with the dimension of 1 × 138).
9) The procedure from 5th to 8th was repeated for 50 times to obtain a 50 × 138 classification accuracy matrix. The mean and SEM vectors (1 × 138) of this matrix were used to plot fig. S33, S34.

To generate the shuffled data, the IDs of odor were randomly re-assigned in the third step to generate shuffled templates. Other procedures were followed as previously to generate the mean and SEM

vectors of classification accuracy matrix for shuffled data, also plotted in fig. S33, S34. The Mann-Whitney U-test ($p < 0.05$ as the criterion) was used for the statistical significance test, as marked in fig. S33, S34.

Analysis: Correlation between performance and odor selectivity

Euclidian distance was calculated to quantify odor selectivity for each neuron (Fig. 4H, fig. S28). The firing rates in delay-period were binned (size: one second) in each trial to form an activity vector. The median of all the activity vectors following a particular odor sample was defined as the center for the corresponding sample. Higher distance between the centers indicated for larger odor selectivity. Therefore the Euclidian distance between centers following different odor samples was calculated as the raw selectivity index, and then normalized by subtracting the activity distance before odor sample delivery (4 sec in duration). The resulting normalized Euclidian distance was averaged across neurons recorded simultaneously from one mouse in a particular day in learning to represent odor selectivity of a given mouse. Performance of mice for each day was then plotted against odor selectivity for Fig. 4H, with each dot indicated for performance and odor selectivity of one mouse. Linear regression was performed and correlation coefficient between odor selectivity and performance were calculated. To test the statistical significance of the correlation, bootstrap analysis of correlation coefficient was performed for 100 times. The 95% confidence interval ($p < 0.05$) was reported in Fig. 4H.

Figures S1-S19

Fig. S1

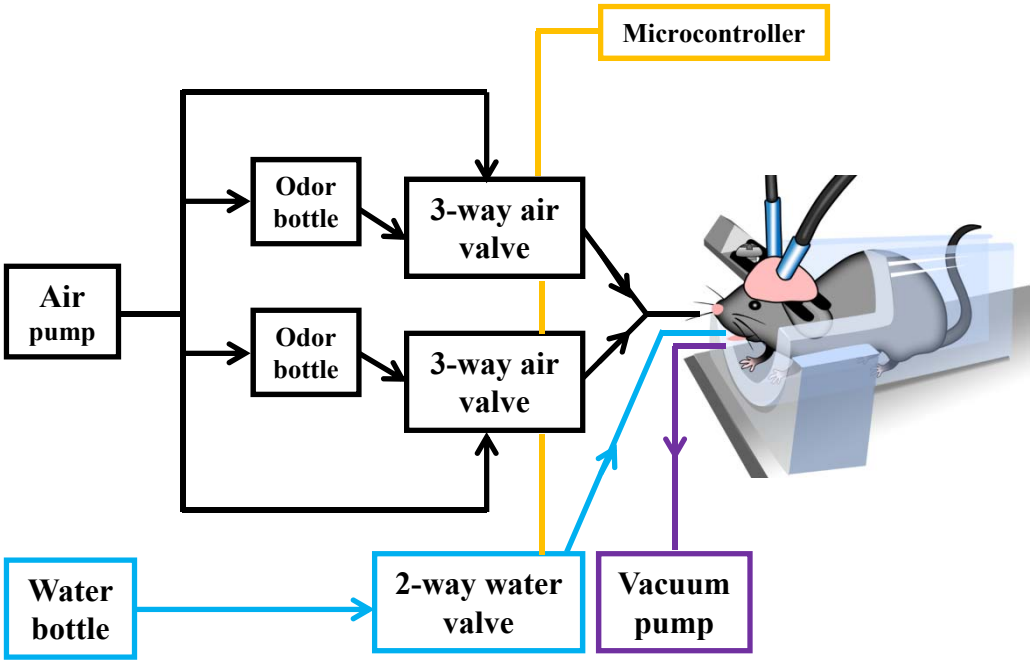

Fig. S1. Schematic diagram of behavior training setup for olfactory delayed non-match to sample (DNMS) task.

Fig. S2

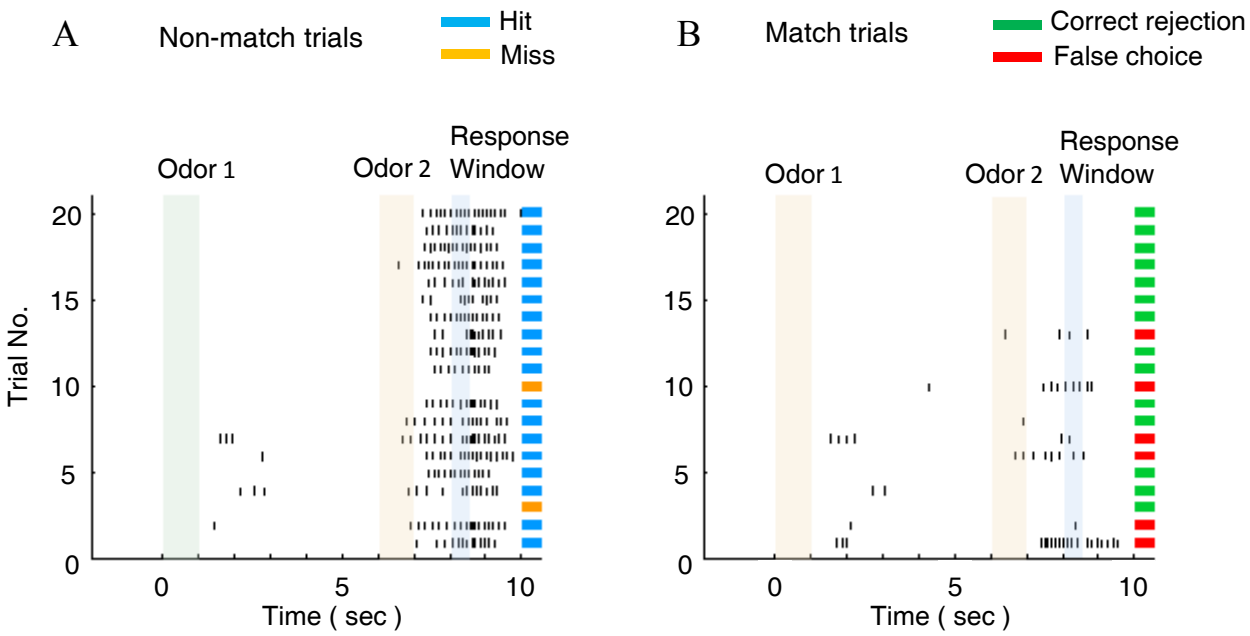

Fig. S2. Example of licking behavior and definition of the trial types. Licking behavior of a control mouse in 20 non-match **(A)** or match **(B)** trials, evenly selected across five days in learning. Each tick represents a licking event. Colored areas corresponded to the two odor delivery periods and the response time window, as indicated above.

Fig. S3

A B

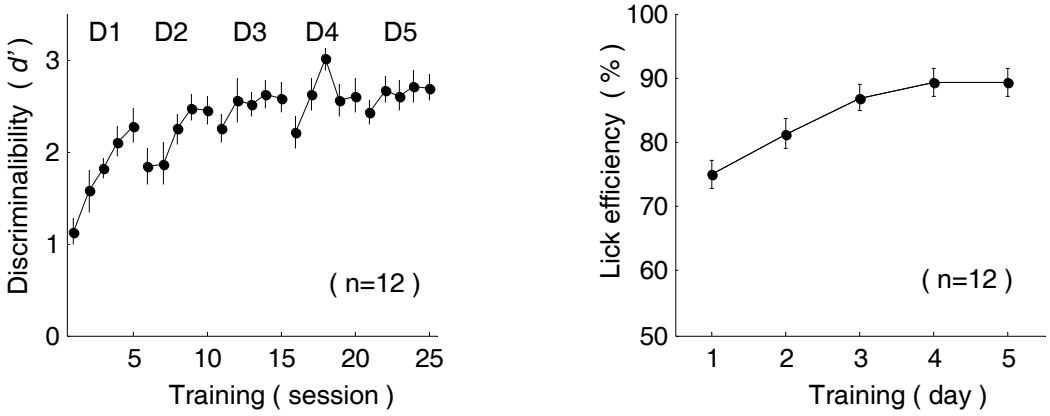

Fig. S3. The learning process of olfactory delayed non-match to sample (DNMS) task. **(A)** Discriminalibility. Error bar: SEM unless stated otherwise. **(B)** Licking efficiency. See the section of "Behavioral training" in the Supplementary Material.

Fig. S4

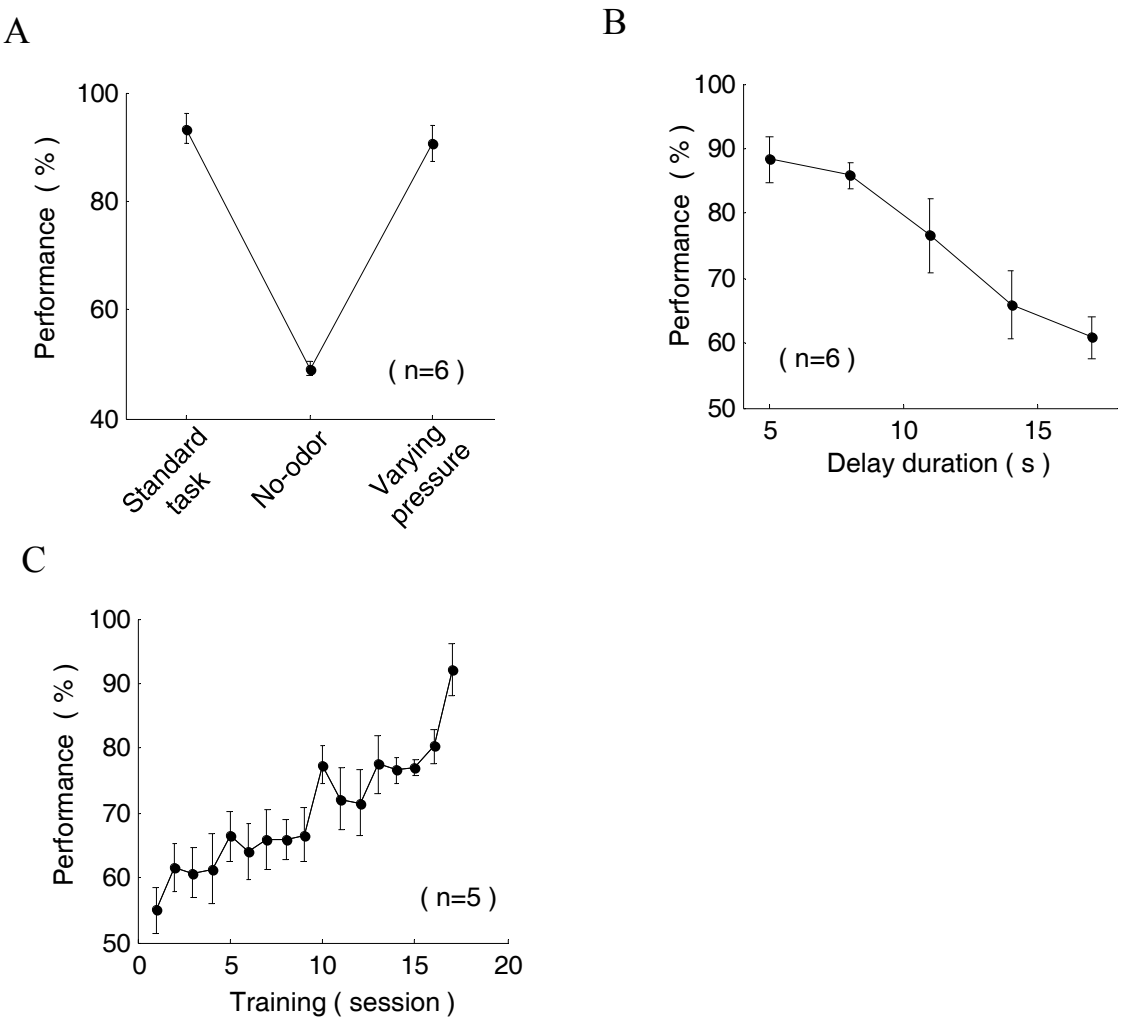

Fig. S4. Validation of the current design as an olfactory working memory task. (A) The behavioral performance under normal, no-odor and varying pressure conditions. Note that mice could not perform the task without olfactory inputs, but could perform the task when the pressure of odor delivery was randomly varied on a trial-by-trial basis. **(B)** The performance in the experiments of varying delay durations. **(C)** The performance in learning of 4-odorant DNMS task within one day, after 2-odorant DNMS task was well-trained.

Fig. S5

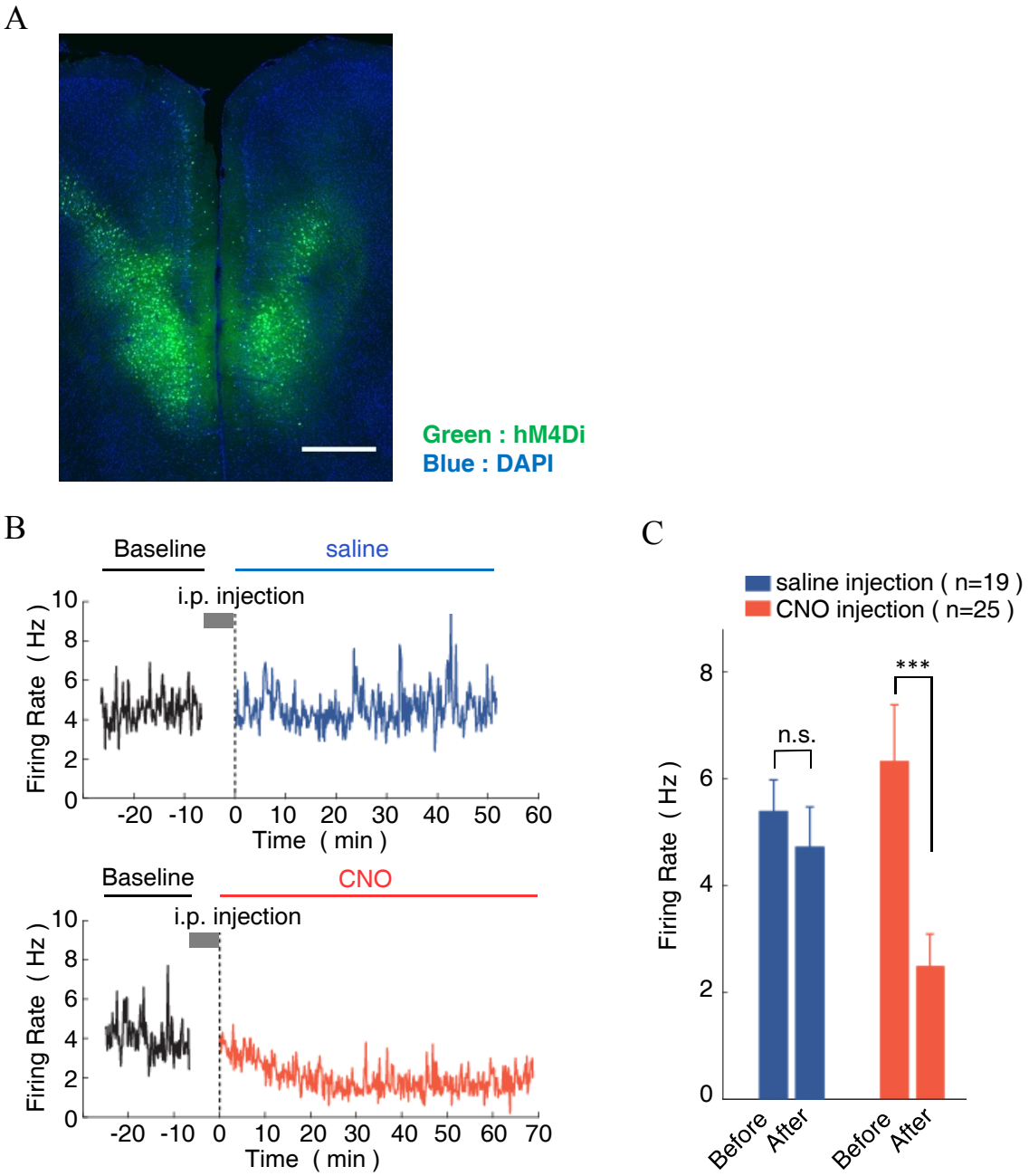

Fig. S5. Expression and functionality verification of hMD4i. (A) Immunostaining evidence of the expression of AAV-hSyn-hM4Di-mCitrine in mPFC of wild-type mice. (scale bar: 500 µm). **(B)** Firing rates of an example neuron with i.p. injection of saline and CNO (1mg/kg b.w.). **(C)** Averaged firing rates of recorded mPFC neurons before and after saline or CNO injection. $p_{saline} > 0.1$; *** $p_{CNO} < 0.001$, Mann-Whitney U-test.

Fig. S6

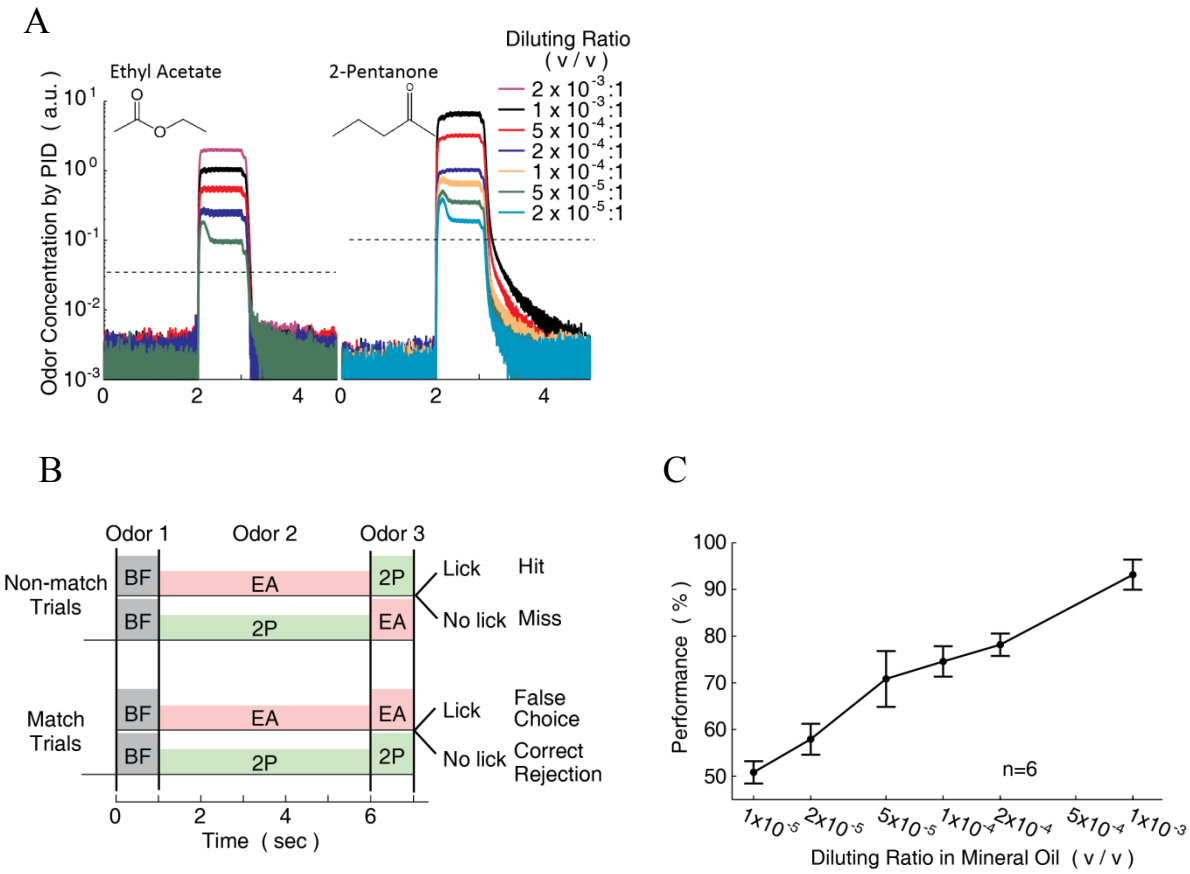

Fig. S6. Paradigm and results for the control experiments to exclude the possibility that mice were using residual odor during the delay period to perform the WM task. (A) Task related odor concentration measured by photoionization detector (PID). Broken lines: behavioral threshold of chance-level performance in C. **(B)** Non-match to long duration sample (NMLS) task diagram. BF, butyl format, as a trial starting cue. EA, ethyl acetate; 2P, 2-pentanone. The concentration of odor 2 (sample) was systematically varied. **(C)** Performance in NMLS task with varying sample concentration.

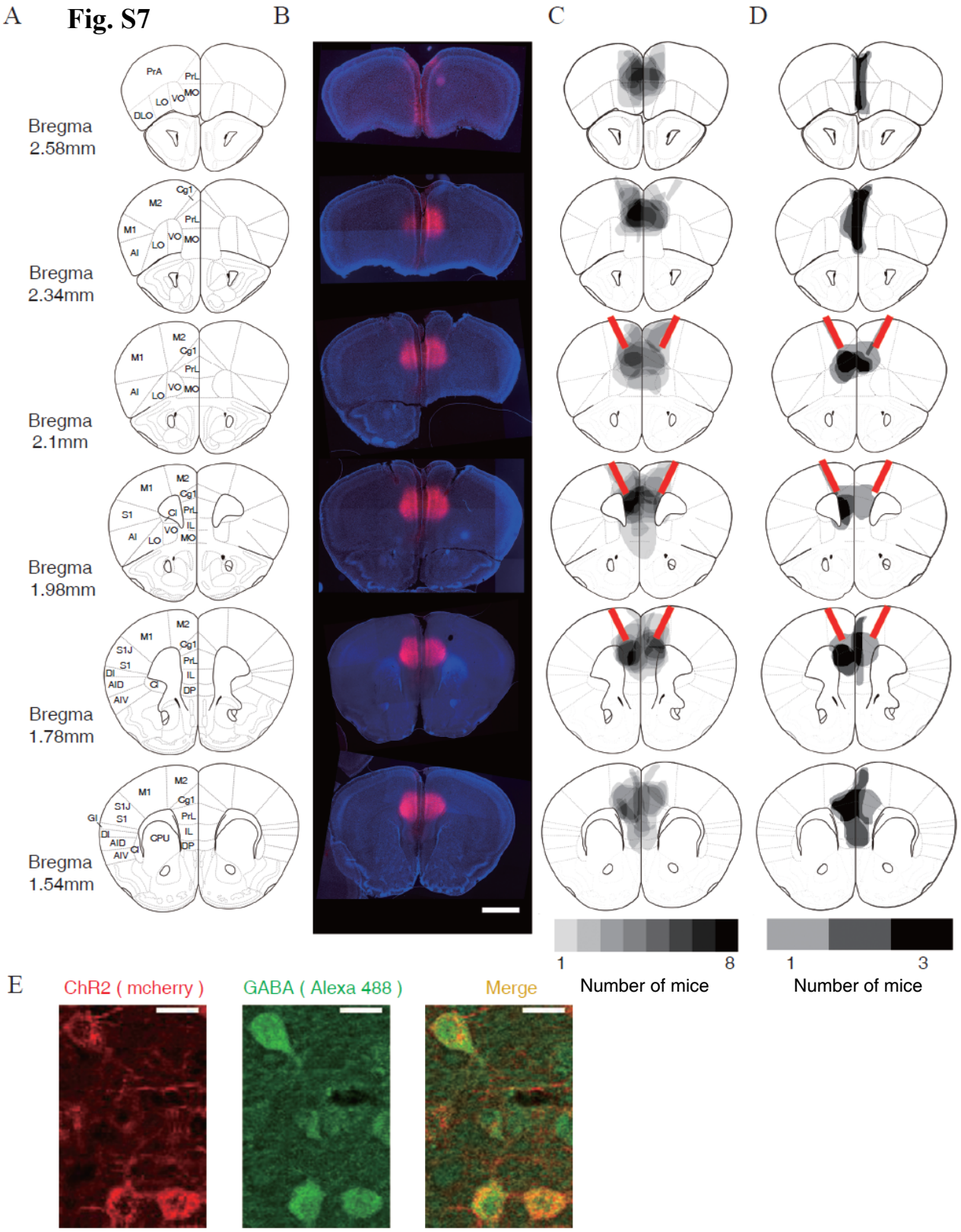

Fig. S7. Immunostaining evidence of the expression of AAV-DIO-ChR2 in mPFC of VGAT-Cre mice. (A) Schematics showing subregions of mPFC (including prelimbic area, PL, infralimbic area, IL, anterior cingulate cortex, ACC, marked as Cg1) from anterior to posterior locations. **(B)** Example brain slices from a VGAT-Cre mouse expressed with AAV-DIO-ChR2-mcherry. Scale bar: 1000 μm. **(C)** Overlay of DIO-ChR2 expression in 8 mice. Darkness of certain areas indicates number of mice expressed virus in that area. **(D)** Overlay of DIO-mcherry expression in 3 mice. Red bars in **(C)** and **(D)**: locations of optical fibers. **(E)** Enlarged images of ChR2 expression. Scale bar: 20 μm.

Fig. S8

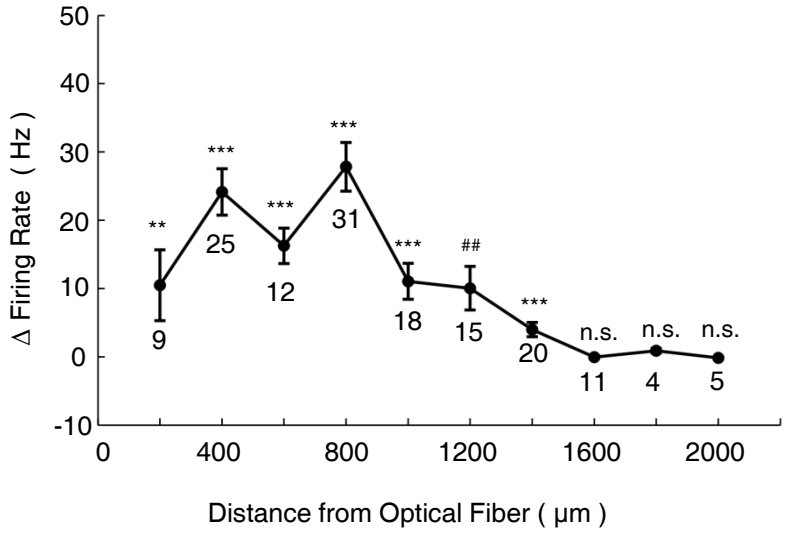

Fig. S8. Spatial range of optogenetic manipulation. Δ Firing rates (for difference between laser-on and –off periods) for neurons expressing ChR2 were plotted against distances of recording electrodes from optical fiber. Experiments were operated on C57 mouse expressed with AAV-CaMKIIα-ChR2 virus. Laser-on protocol: 473 nm, 2 mW, step illumination of 2 sec in duration. Marked above each data point was the significance level for difference between laser-on and –off periods (***, $p < 0.001$; **, $p=0.008$; ##, $p=0.002$; Wilcoxon signed rank test). Marked below each data point were numbers of neurons for each recording site were marked below each data point.

Fig. S9

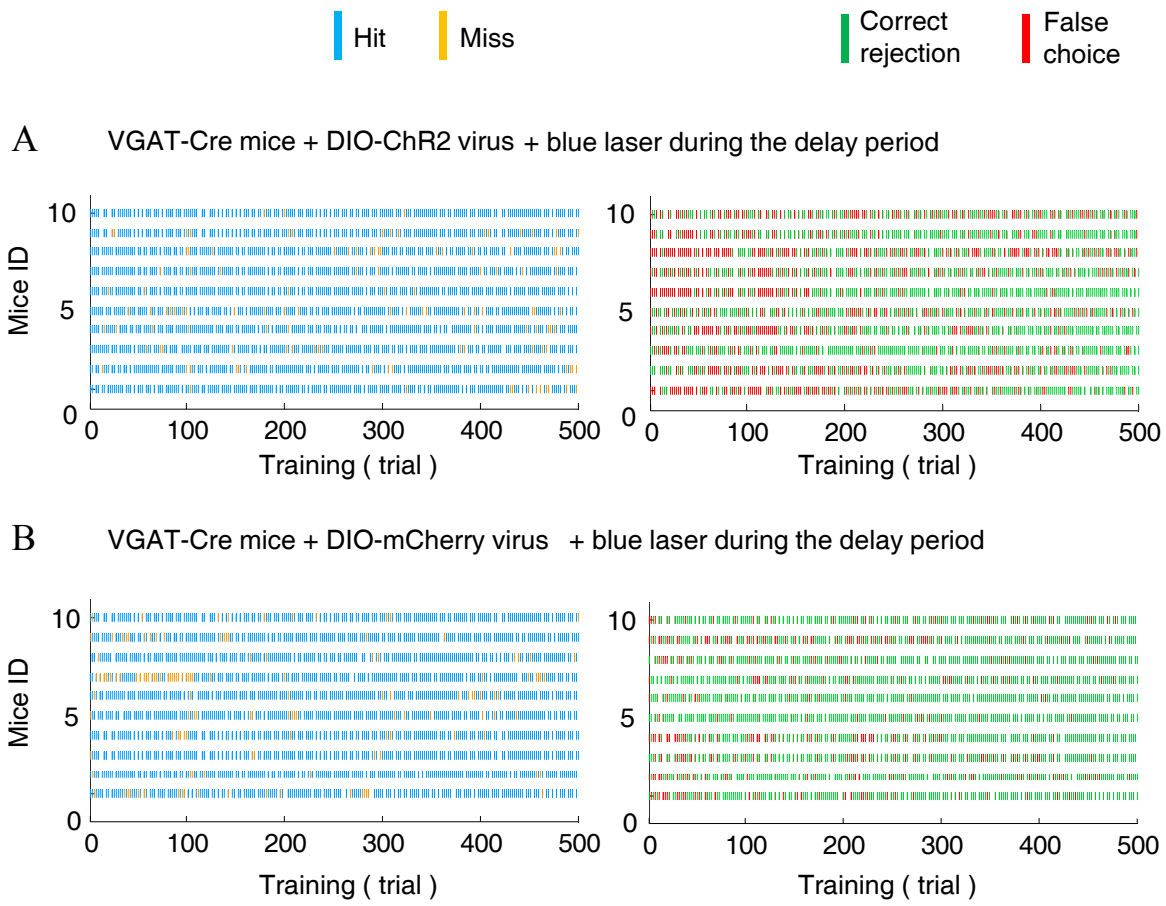

Fig. S9. Performance of all mice in the experiments of optogenetic suppression of mPFC pyramidal neurons during the delay period. (A) Raster plots of performance for all the VGAT-Cre mice expressed with AAV-DIO-ChR2 (n=10), with blue laser illumination during the delay period. **(B)** Raster plots of performance for all the VGAT-Cre mice expressed with AAV-DIO-mCherry as control in the blind design (n=10), with blue laser illumination during the delay period. Each mice experienced 5 days of training, 100 trials per day (50 match and 50 non-match trials).

Fig. S10

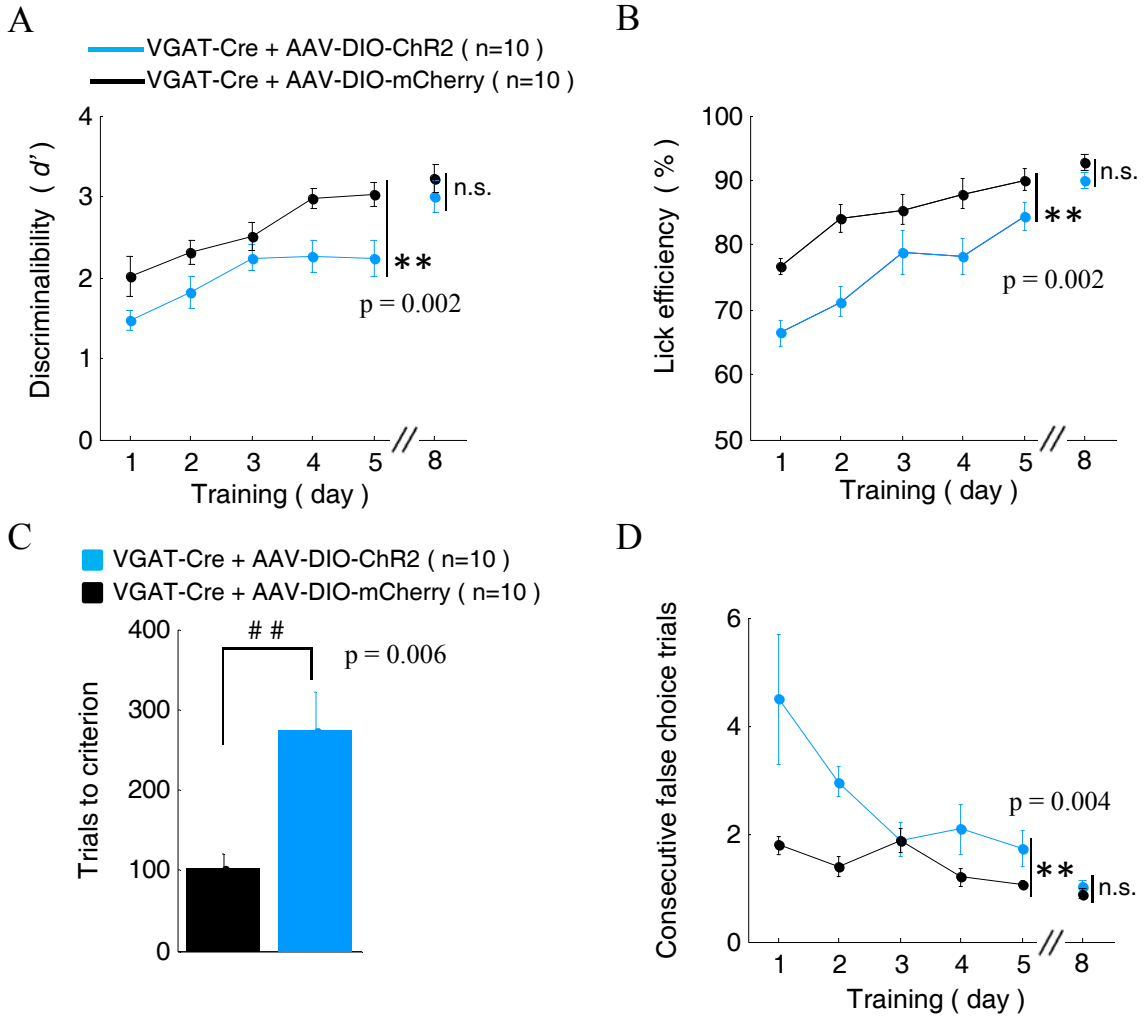

Fig. S10. Suppression of delay-period activity in mPFC by optogenetic activation of GABAergic neurons impaired learning of WM task. (A,B) Discriminalibility and licking efficiency significantly decreased during the learning phase but not after mice were well trained in ChR2 group compared to mCherry group. **(C,D)** Number of trials to criterion (performance reaching 80% in successive 40 trials) and number of consecutive false choice trials significantly increased during learning in ChR2 group compared to mCherry group. ** $p_{ChR2} < 0.01$, two-way ANOVA with mixed design; ## $p < 0.01$, Mann-Whitney U-test. WT, well-trained phase.

Fig. S11

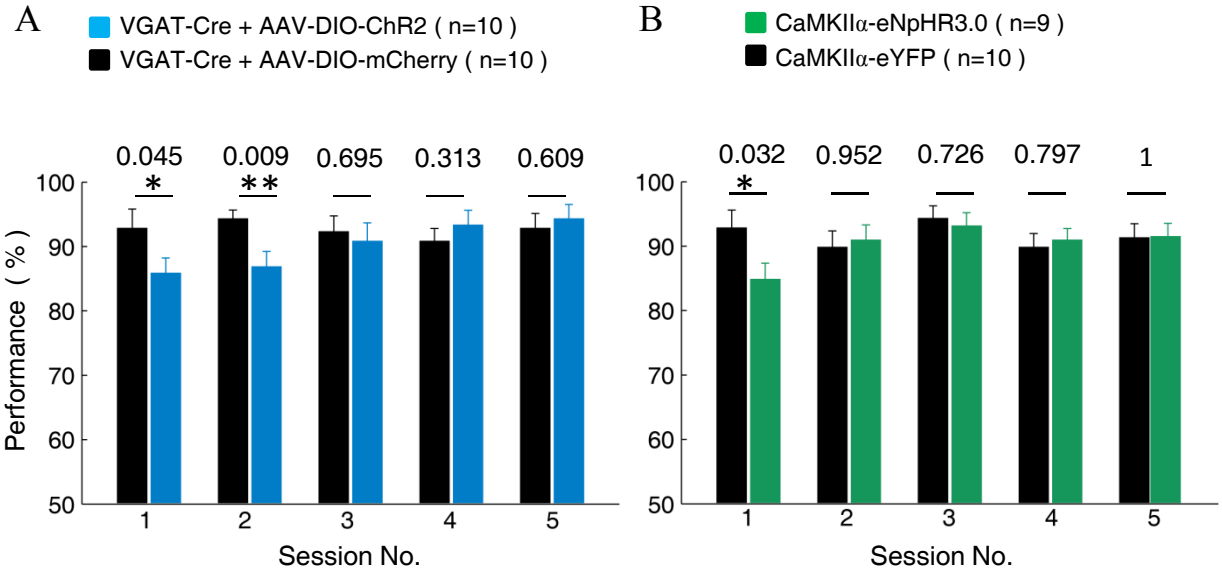

Fig. S11. Session based analysis of behavioral performance in the experiments of suppressing delay-period activity during the well-trained phase. (A) Performance in VGAT-Cre mice expressed with ChR2 or mCherry. Two-way ANOVA with mixed design : $F_{ChR2(1,18)}$=1.543; p_{ChR2}=0.23; $F_{session(4,72)}$=1.396; $p_{session}$=0.244; $F_{interaction(4,72)}$=2.984; $p_{interaction}$= 0.024; **(B)** Performance in wild-type mice injected with NpHR or eYFP viruses. Two-way ANOVA with mixed design : $F_{NpHR(1,17)}$=1.14; p_{NpHR}=0.301; $F_{session(4,68)}$=1.481; $p_{session}$=0.218; $F_{interaction(4,68)}$=1.65; $p_{interaction}$=0.172. Values above bars: p values of Mann-Whitney U-test between virus groups for corresponding session, without correction for multiple comparison.

Fig. S12

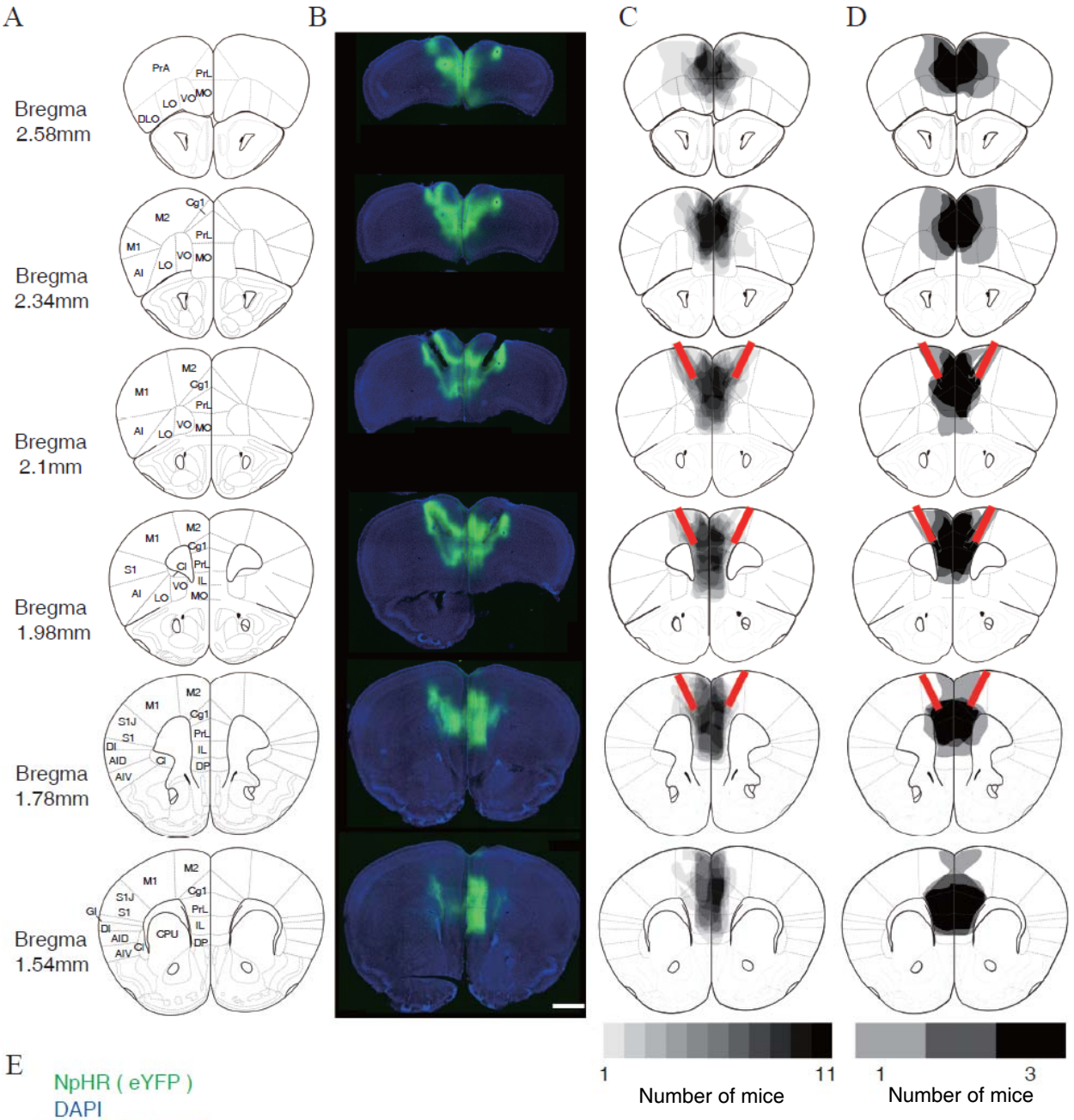

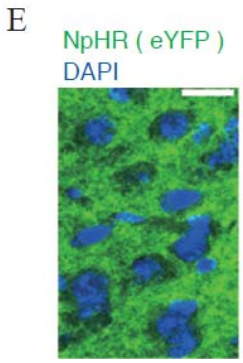

Fig. S12. Immunostaining evidence of the expression of AAV-CaMKIIα-eNpHR3.0 in mPFC of wild type mice. (A) Schematics showing subregions of mPFC from anterior to posterior locations. **(B)** Example brain slices from a C57 mouse expressed with AAV-CaMKIIα-NpHR-eYFP. Scale bar: 1000 μm. **(C)** Overlay of CaMKIIα-NpHR-eYFP expression in 11 mice. Darkness of certain areas indicates number of mice expressed virus in that area. **(D)** Overlay of CaMKIIα-eYFP expression in 3 mice. Red bars in **(C)** and **(D)**: locations of optical fibers. **(E)** Enlarged image of NpHR expression. Scale bar: 20 μm.

Fig. S13

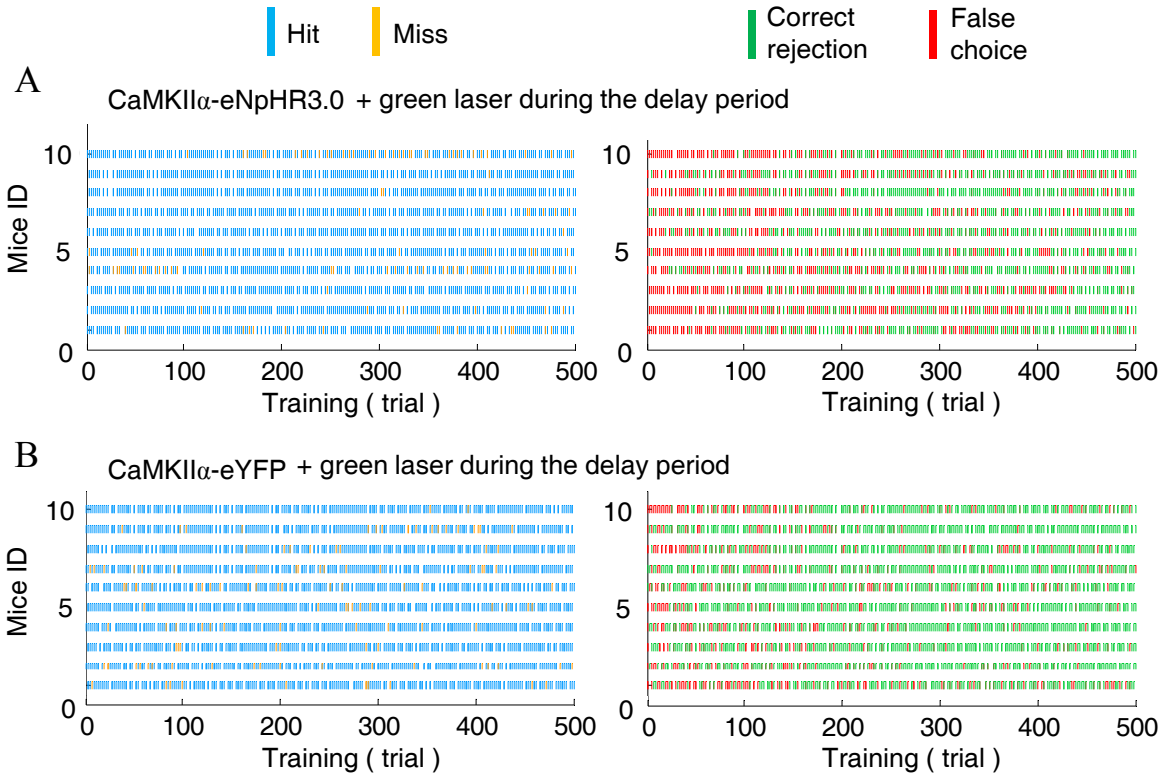

Fig. S13. Performance of all mice in experiments of direct optogenetic suppression of mPFC pyramidal neurons during delay period. **(A)** Raster plots of performance for all the wild-type mice injected AAV-CaMKIIα-eNpHR3.0 (n=10), with green laser illumination during the delay period. **(B)** Raster plots of performance for all the control wild-type mice expressing AAV-CaMKIIα-eYFP (n=10), with green laser illumination during the delay period. Note that each mice experienced 5 days of training, 100 trials per day (50 match and 50 non-match trials).

Fig. S14

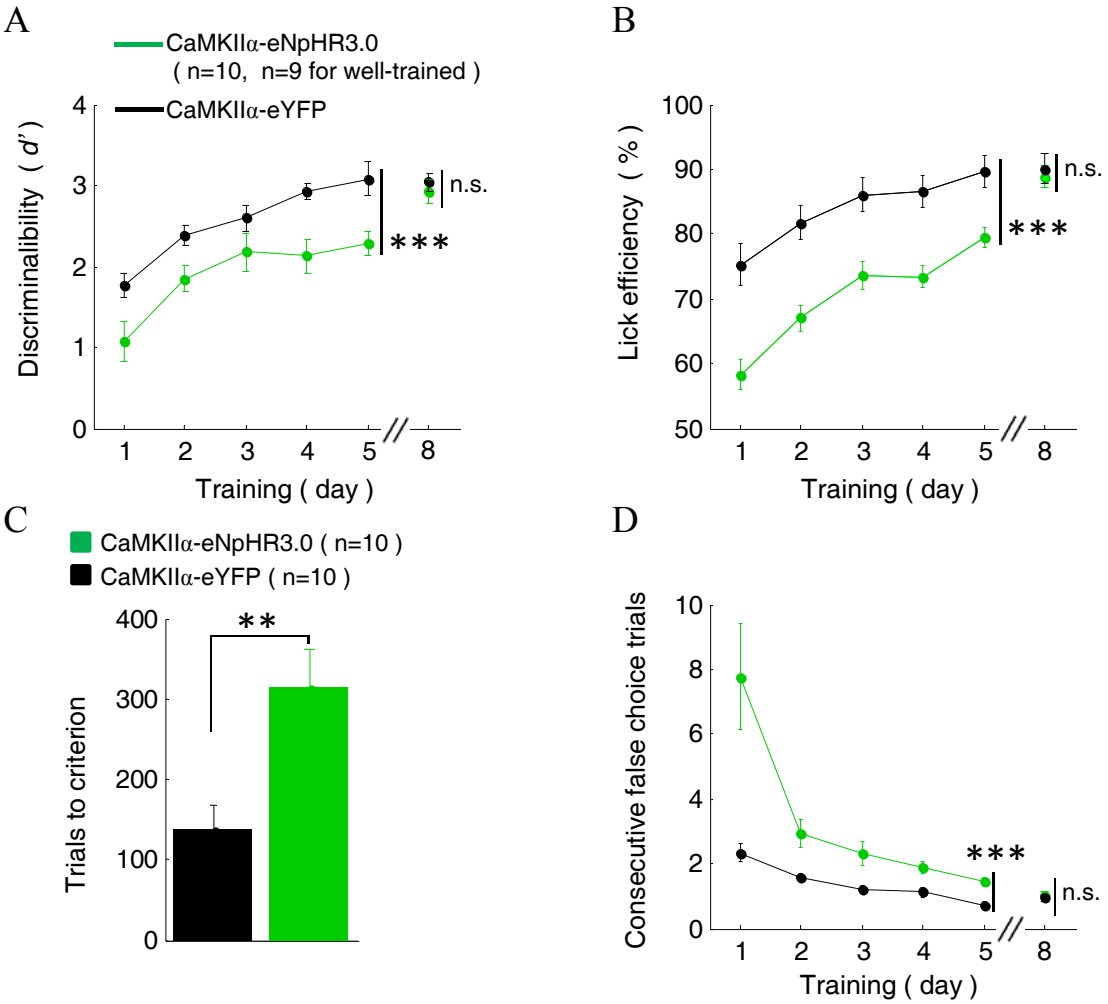

Fig. S14. Suppression of delay-period activity in mPFC by optogenetic inhibition of pyramidal neurons impaired learning of WM task. (A,B) Discriminalibility and licking efficiency were significantly decreased during learning in NpHR group compared to eYFP group. **(C,D)** Number of trials to criterion (performance reaching 80% in successive 40 trials) and number of consecutive false choice trials were significantly increased during learning in NpHR group compared to eYFP group. *** $p_{NpHR} < 0.001$, two-way ANOVA with mixed design; ** $p = 0.0013$, Mann-Whitney U-test.

Fig. S15

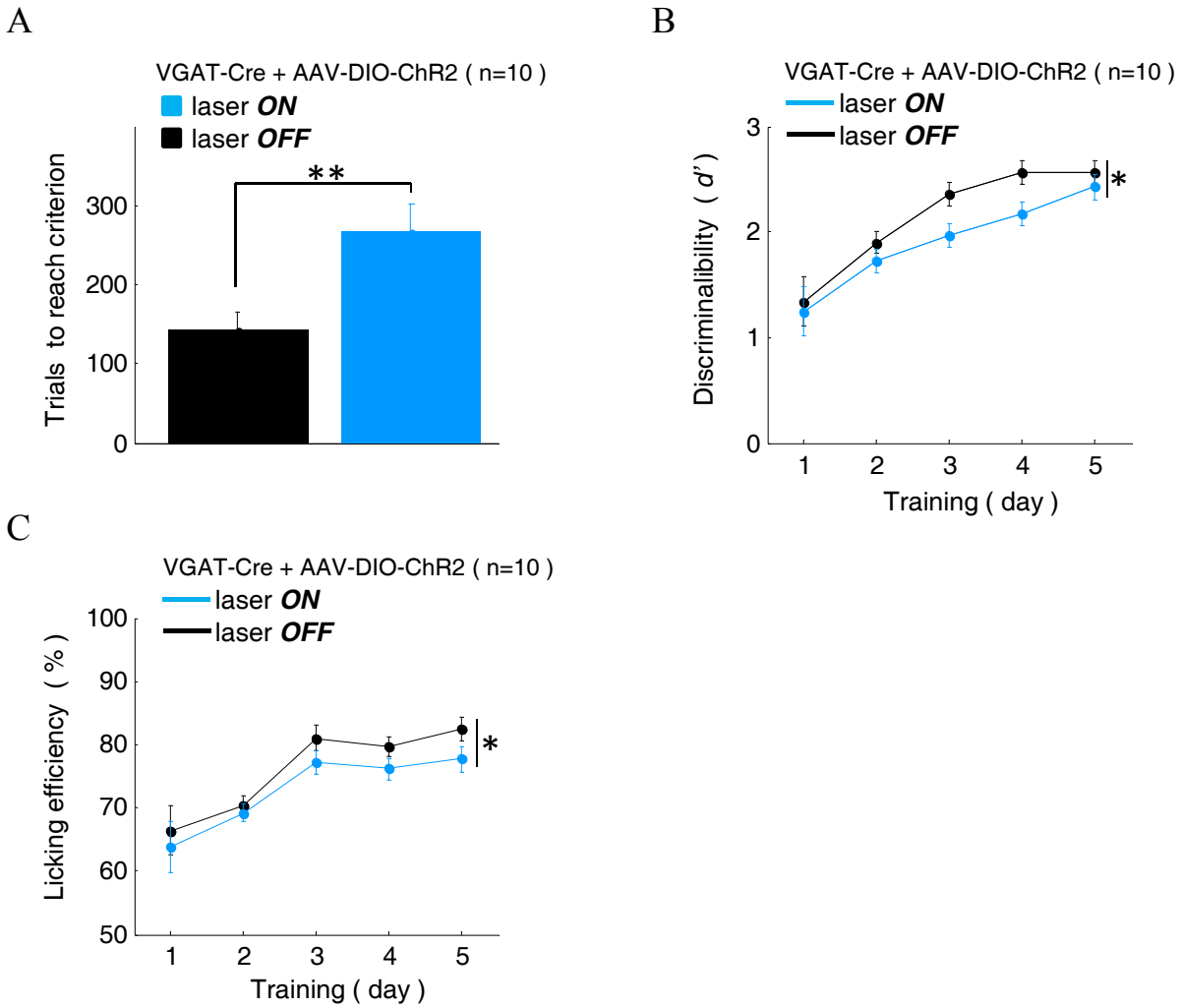

Fig. S15. Suppression of mPFC delay-period activity by optogenetic manipulation impaired learning of the WM task on a trial-by-trial basis. (A) Number of trials to criterion (performance reaching 80% in successive 40 trials) in laser-on and -off trials for VGAT-Cre mice expressed with AAV-DIO-ChR2. ** $p = 0.0086$, Mann-Whitney U-test. **(B)** Discriminalibility. * $p_{laser} = 0.02$, two-way ANOVA with mixed design. **(C)** Licking efficiency. * $p = 0.038$, two-way ANOVA with mixed design.

Fig. S16

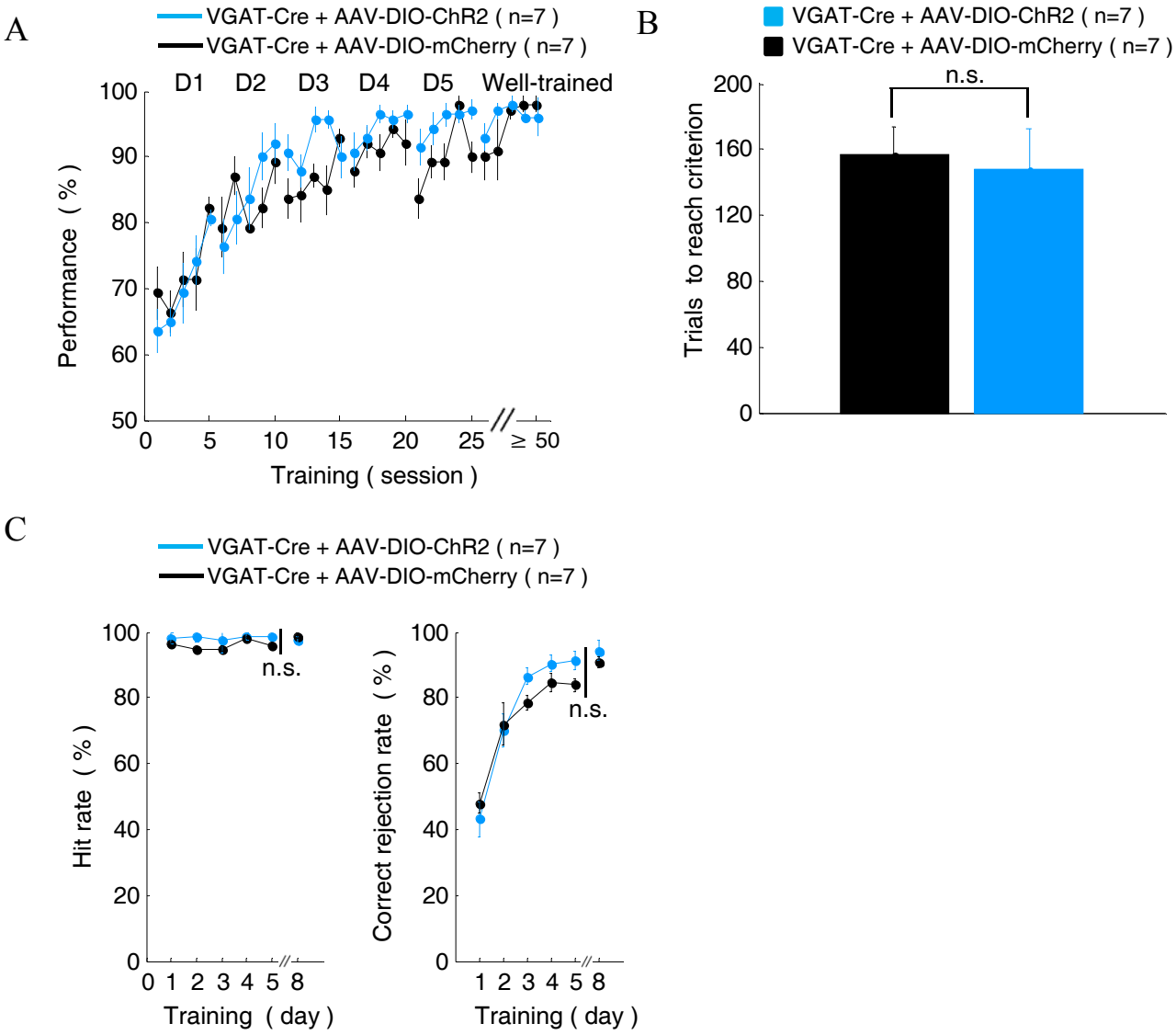

Fig. S16. Suppression of delay-period activity in the somatosensory cortex (S1) did not impair learning of olfactory WM task. (A) Performance. Statistics: two-way ANOVA with mixed design. **(B)** Number of trials to criterion (performance reaching 80% in successive 40 trials). Statistics: Mann-Whitney U-test. **(C)** Hit and correct rejection rates. Statistics as in A.

Fig. S17

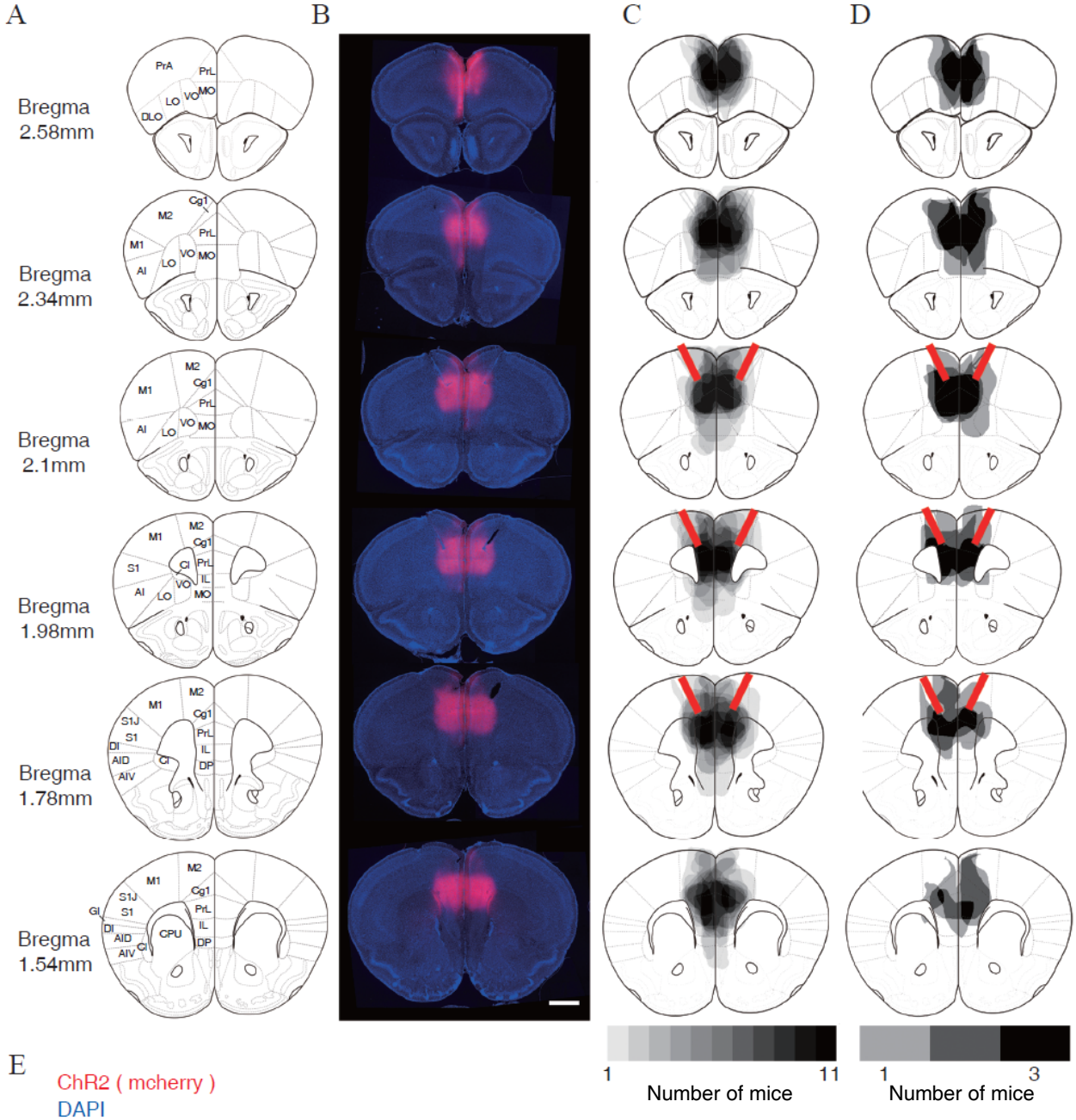

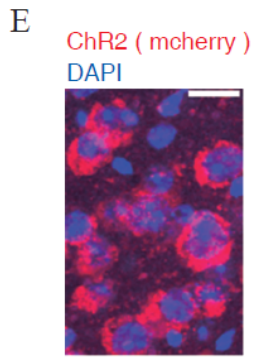

Fig. S17. Immunostaining evidence of the expression of AAV-CaMKIIα-ChR2 in mPFC of wild type mice. (A) Schematics showing subregions of mPFC from anterior to posterior locations. **(B)** Example brain slices from a C57 mouse expressed with AAV-CaMKIIα-ChR2-mcherry. Scale bar: 1000 μm. **(C)** Overlay of CaMKIIα-ChR2 expression in 11 mice. Darkness of certain areas indicates number of mice expressed virus in that area. **(D)** Overlay of CaMKIIα-mcherry expression in 3 mice. Red bars in **(C)** and **(D):** locations of optical fibers. **(E)** Enlarged image of ChR2 expression. Scale bar: 20 μm.

Fig. S18

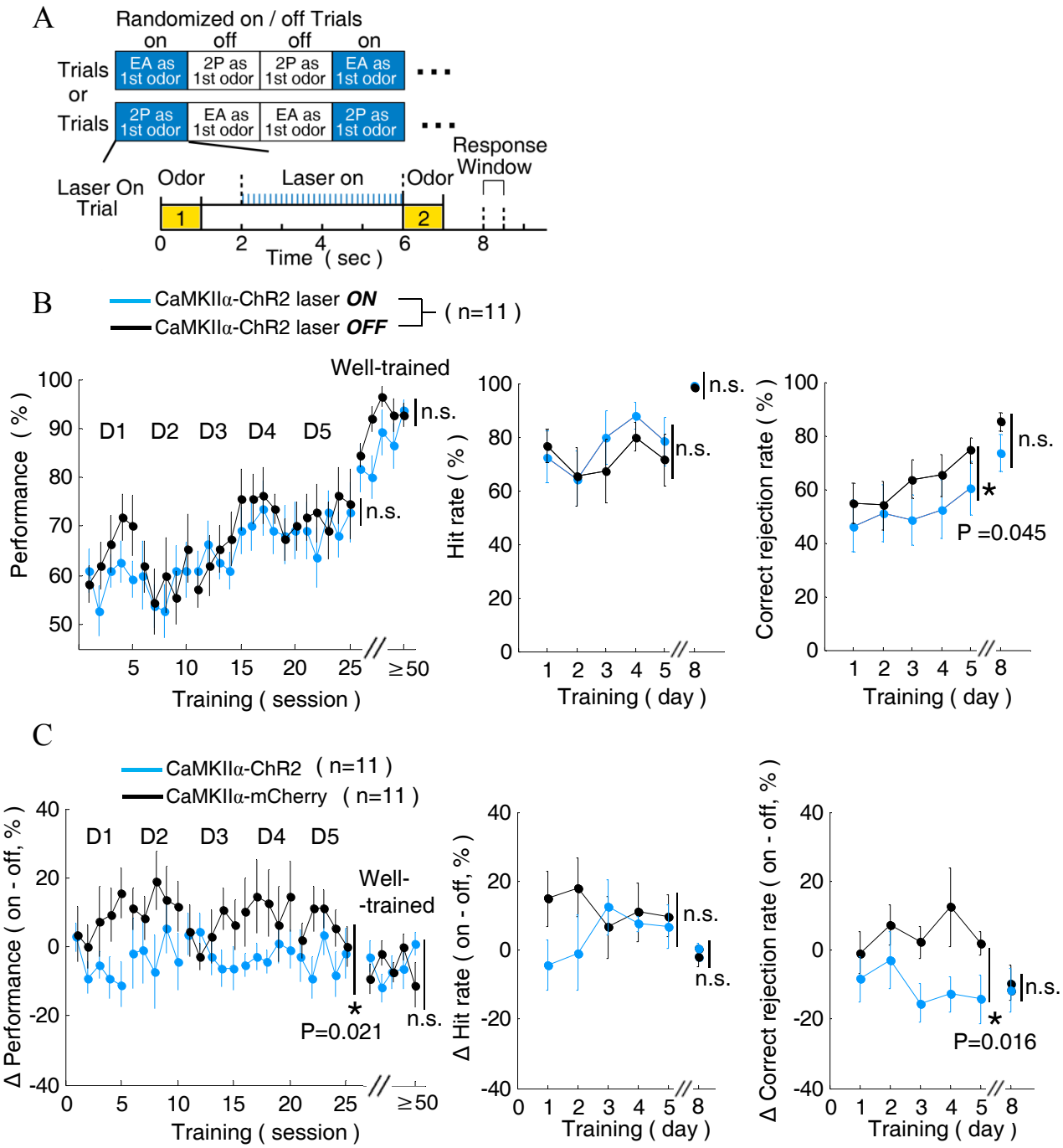

Fig. S18. Paradigm and behavioral performance in the experiments of enhancing mPFC activity during the delay period in an interleaved laser on/off design. (A) Paradigm information. The laser pulse width was 20 ms. **(B)** Performance, hit and correct rejection rates for opto-enhancement in wild-type mice expressed with CaMKIIα-ChR2. **(C)** **Δ**Performance, **Δ**hit, and **Δ**correct rejection rates (laser-on subtracted by laser-off trials) for opto-enhancement experiment in wild-type mice expressed with CaMKIIα-ChR2 and CaMKIIα-mCherry. Statistics: two-way ANOVA with mixed design.

Fig. S19

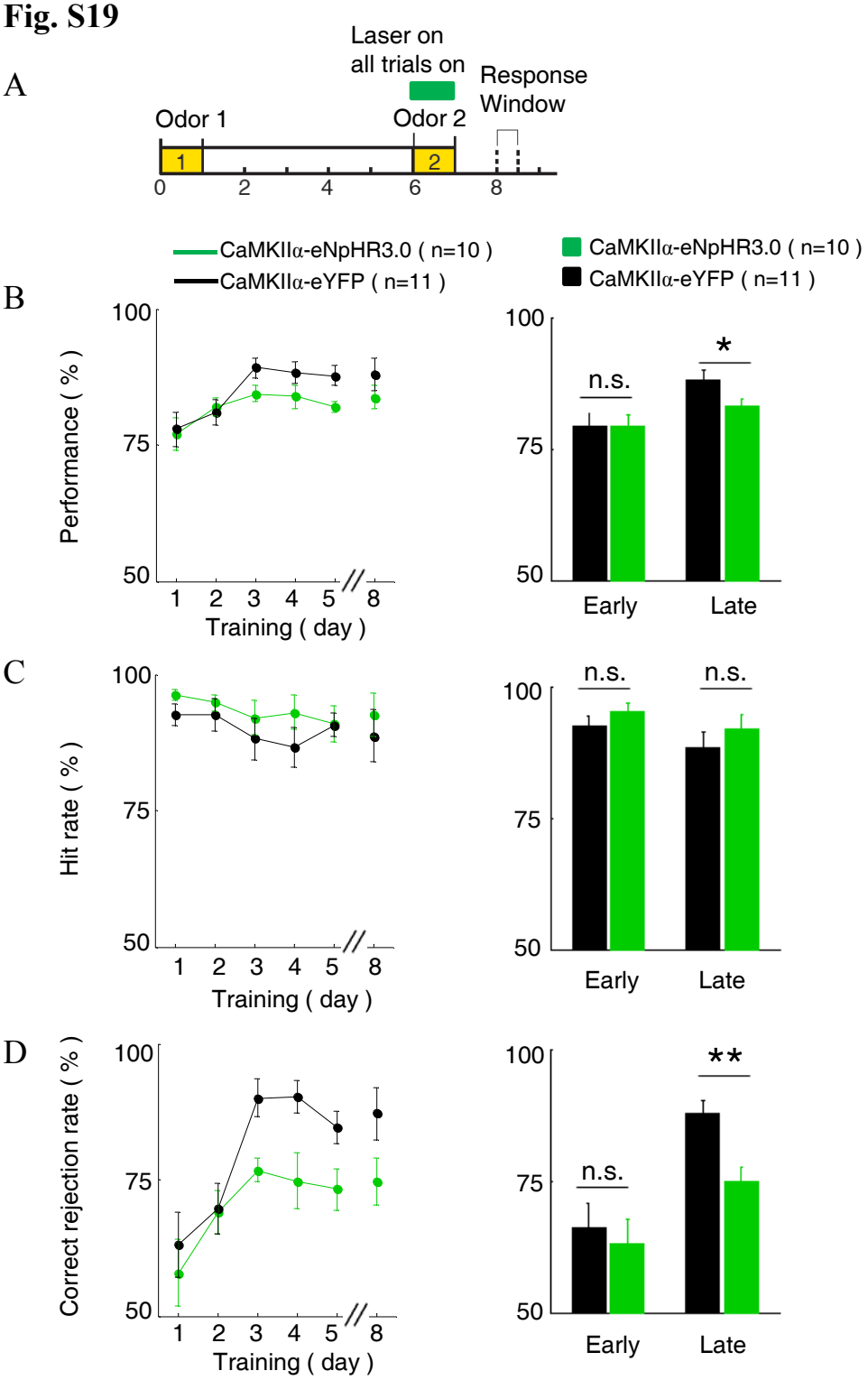

Fig. S19. Behavioral performance for the experiments of optogenetically suppressing mPFC activity during the second odor delivery period in DNMS task. (A) Paradigm information. **(B)** Performance. Early: Day 1 and 2. Late: Day 3 to 5 and well-trained phase (Day 8). *, p = 0.0246, student's t-test. Normal distribution tested by Chi-square goodness-of-fit test. **(C)** Hit rate. **(D)** Correct rejection rate. **, p = 0.002, student's t-test.

Fig. S20

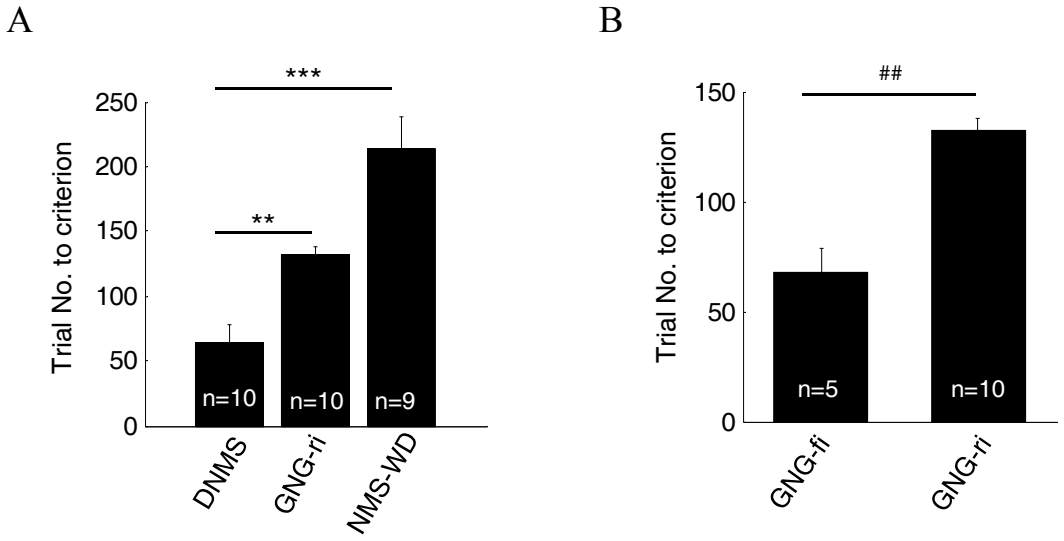

Fig. S20. Comparison among behavioral tasks. (A) Number of trials to criterion (performance reaching 80% in successive 20 trials) of control mice in DNMS, GNG-ri, and NMS-WD tasks. **, p = 0.0026. ***, p =1.3×10^{-4} **(B)** Number of trials to criterion (performance reaching 80% in successive 20 trials) of control mice in GNG-fi and GNG-ri tasks were shown. GNG-fi: Go/No-go task with fixed inter-trial interval, as in fig. S22; GNG-ri: Go/No-go task with random inter-trial interval, as in Fig. 3E. ##, p = 0.0013, Mann-Whitney U-test.

Fig. S21

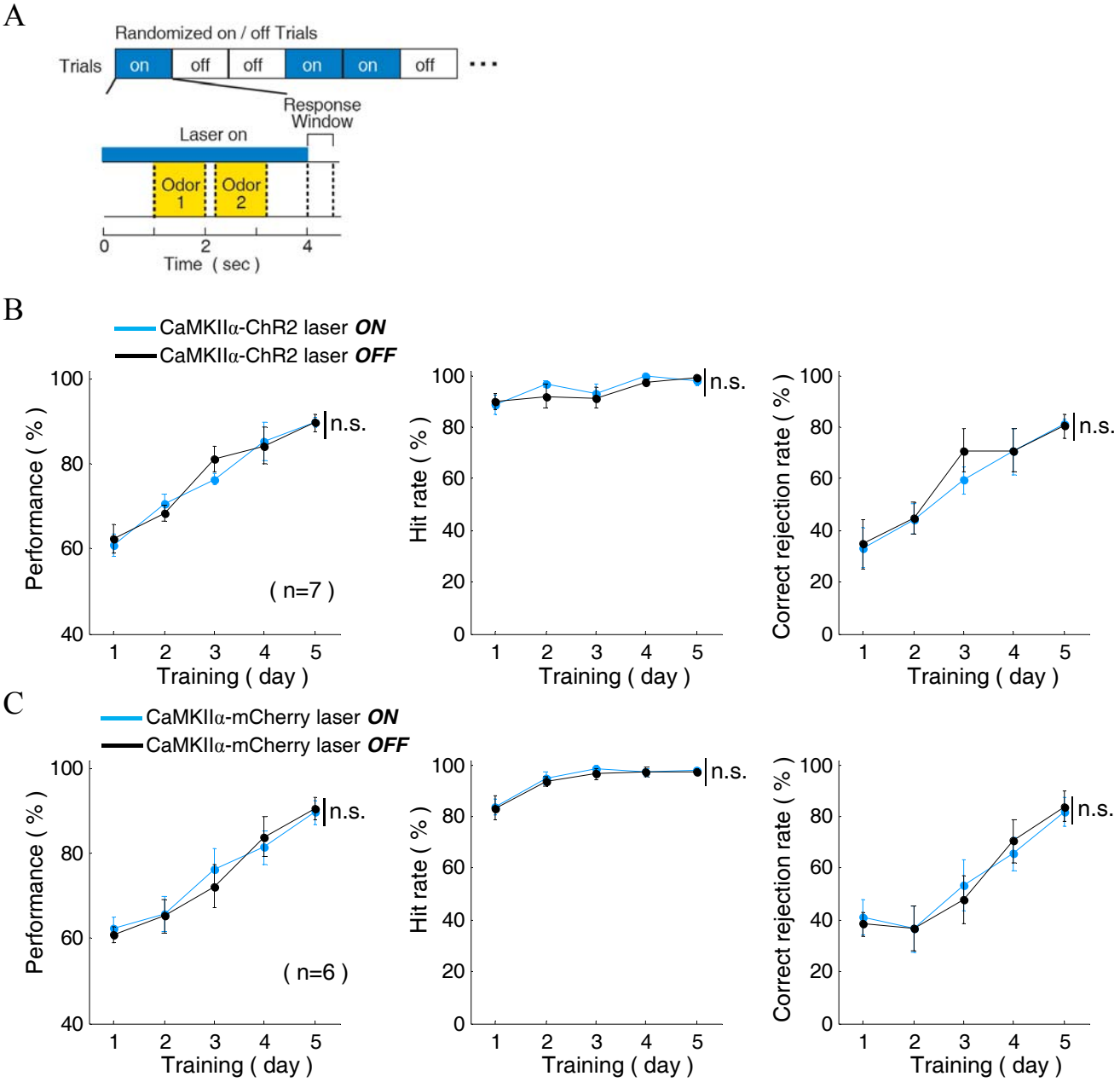

Fig. S21. Paradigm and behavioral performance for the experiments of suppressing mPFC activity in NMS-WD task in the interleaved laser on/off design. (A) Paradigm for NMS-WD task and laser illumination protocol. **(B)** Performance, hit and correct rejection rates in NMS-WD task in laser-on and –off trials for VGAT-Cre mice expressed with AAV-DIO-ChR2. **(C)** Performance, hit and correct rejection rates in NMS-WD task in laser-on and –off trials for VGAT-Cre mice expressed with AAV-DIO-mCherry. Statistics: two-way ANOVA with mixed design.

Fig. S22

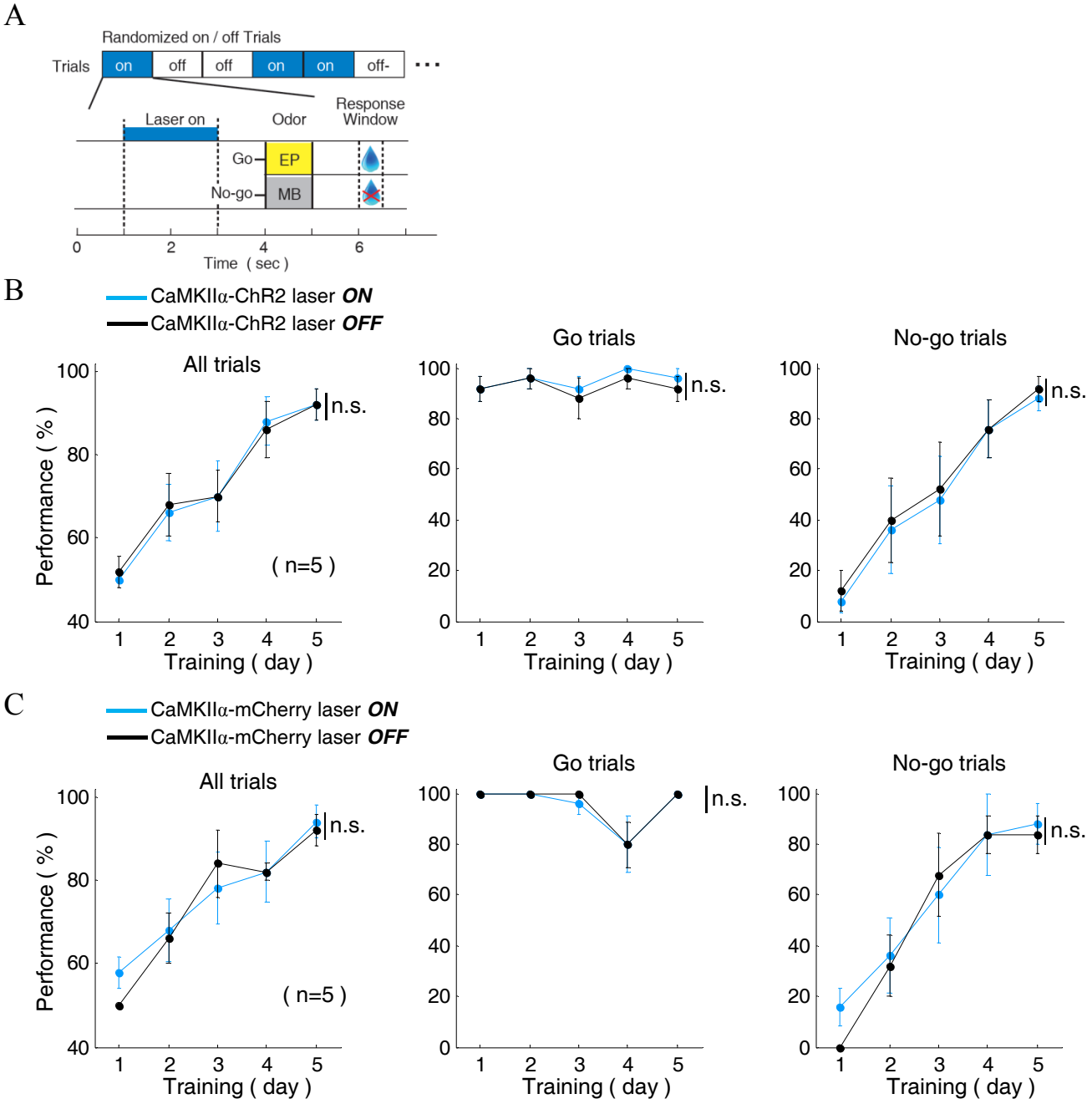

Fig. S22. Paradigm and behavioral performance for the experiments of suppressing mPFC activity in Go/No-go task with fixed inter-trial interval (GNG-fi) in the interleaved laser on/off design. (A) Paradigm for GNG-fi task and laser illumination protocol. The GNG-fi task was different from that in main text (Fig. 3E), in which inter-trial interval was random and trial-starting cue was present before GNG cues (termed GNG-ri). **(B)** Performance in all trials, Go, and No-go trials for VGAT-Cre mice injected with AAV-DIO-ChR2. **(C)** Performance in all trials, Go, and No-go trials for VGAT-Cre mice injected with AAV-DIO-mCherry. Statistics: two-way ANOVA with mixed design.

Fig. S23

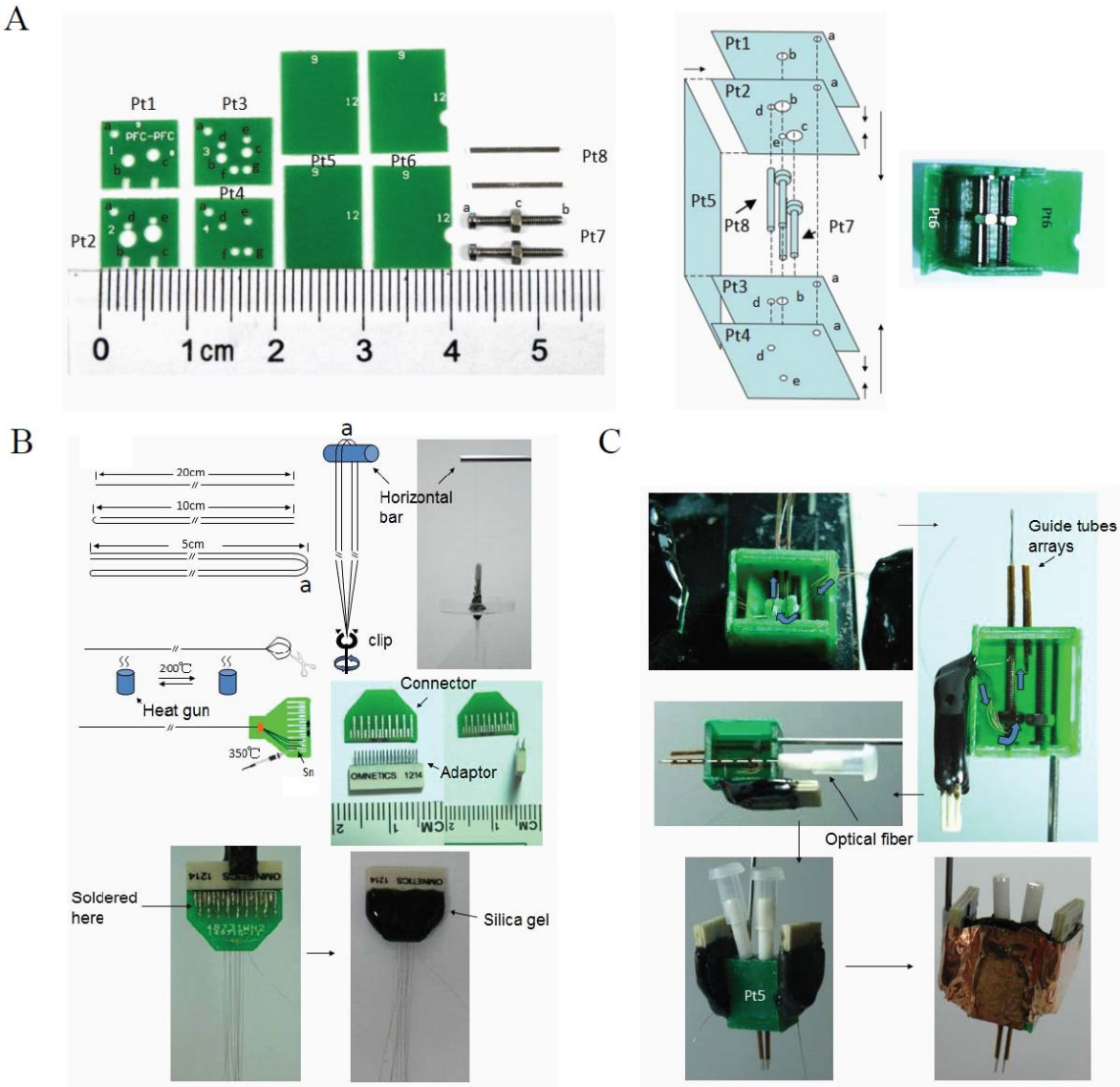

Fig. S23. The procedure for tetrode-microdrive assembly. **(A)** Components and assembling procedure of the micro-drive chamber. **(B)** Tetrode assembling and packaging procedure. **(C)** Assembling procedure of tetrodes, optical fibers (optional for op-tetrode) and micro-drive. Detailed information see the Supplementary Material.

Fig. S24

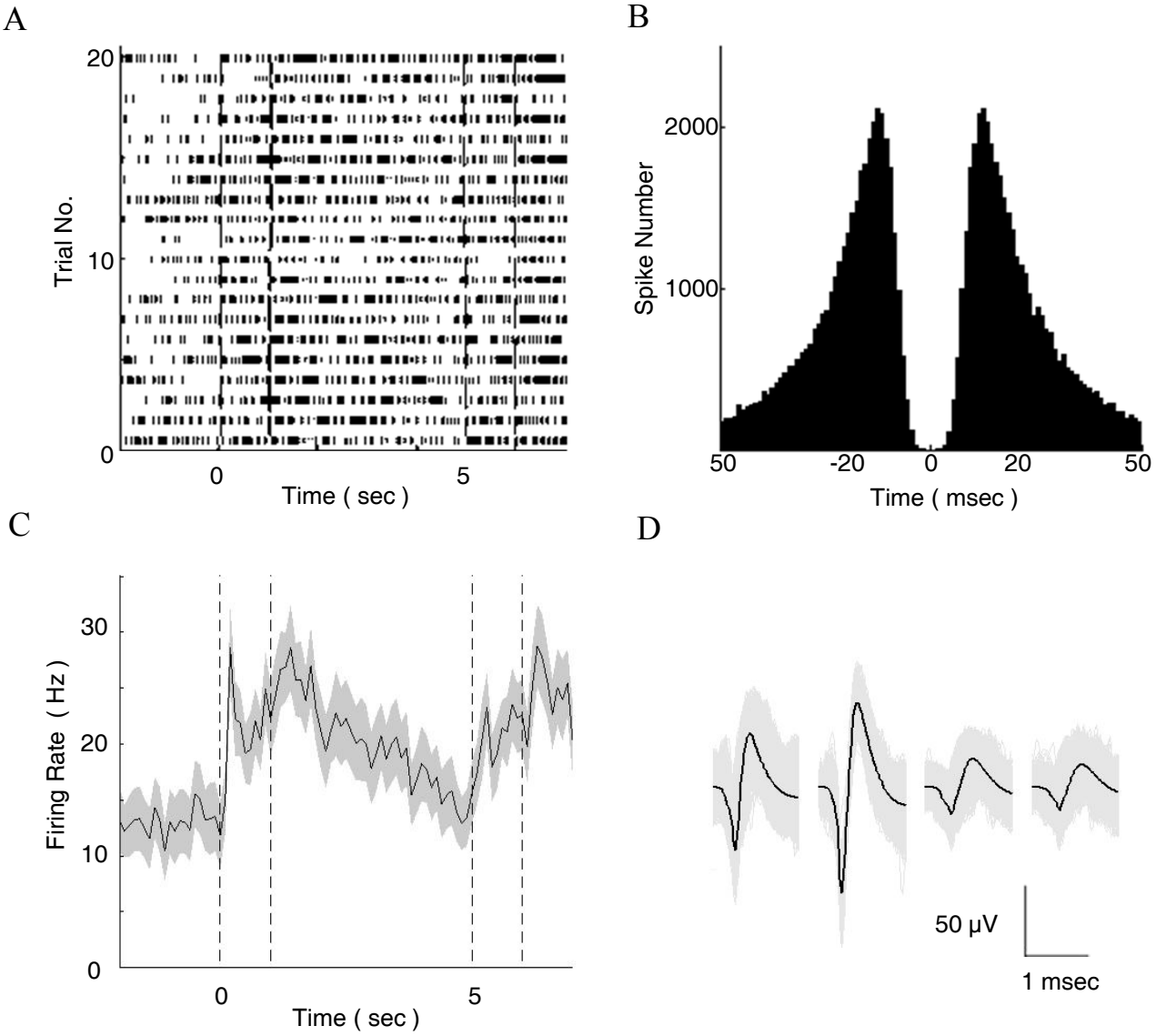

Fig. S24. Example of a recorded single unit. (A) Raster plot. **(B)** Auto-correlogram. **(C)** Averaged firing rate. **(D)** Spike waveforms (averaged in black and separated trials in A in gray).

Fig. S25

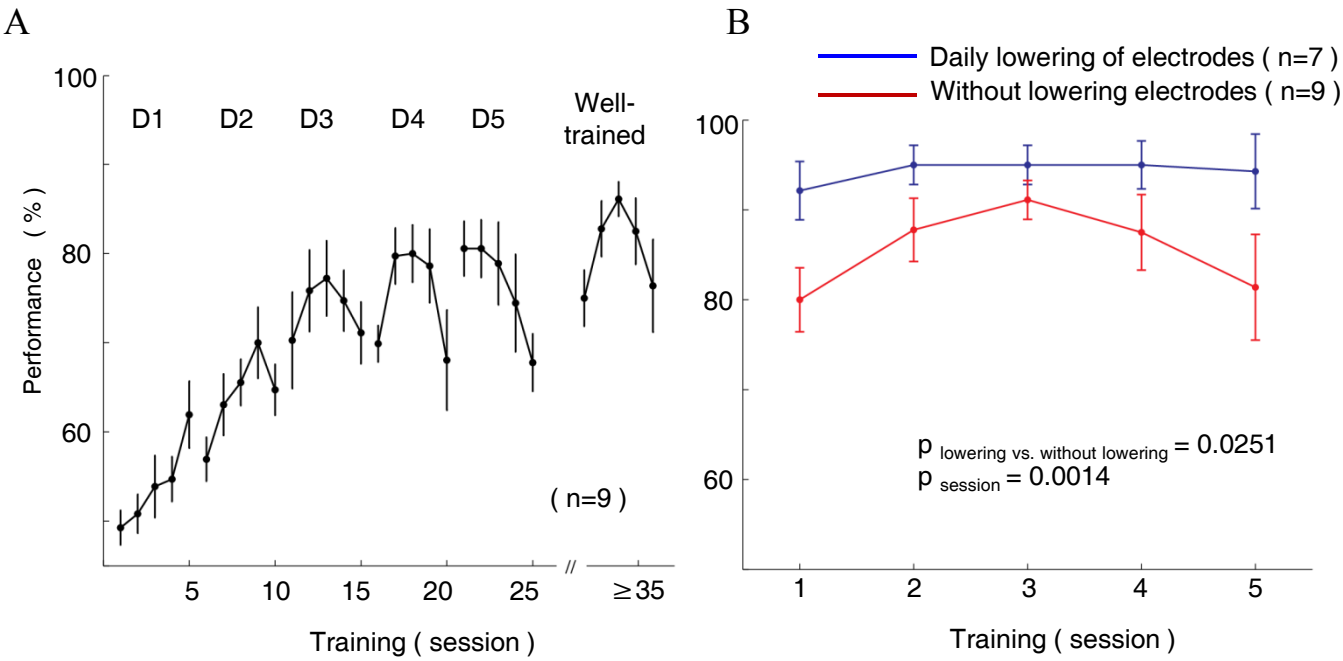

Fig. S25. (A) Behavioral learning curve of recorded mice without daily lowering electrodes. Each session included 40 trials, each day with 5 sessions. **(B)** The comparison between the performance of recorded mice with and without daily lowering of electrodes during the well-trained period. Statistics: two-way ANOVA.

Fig. S26

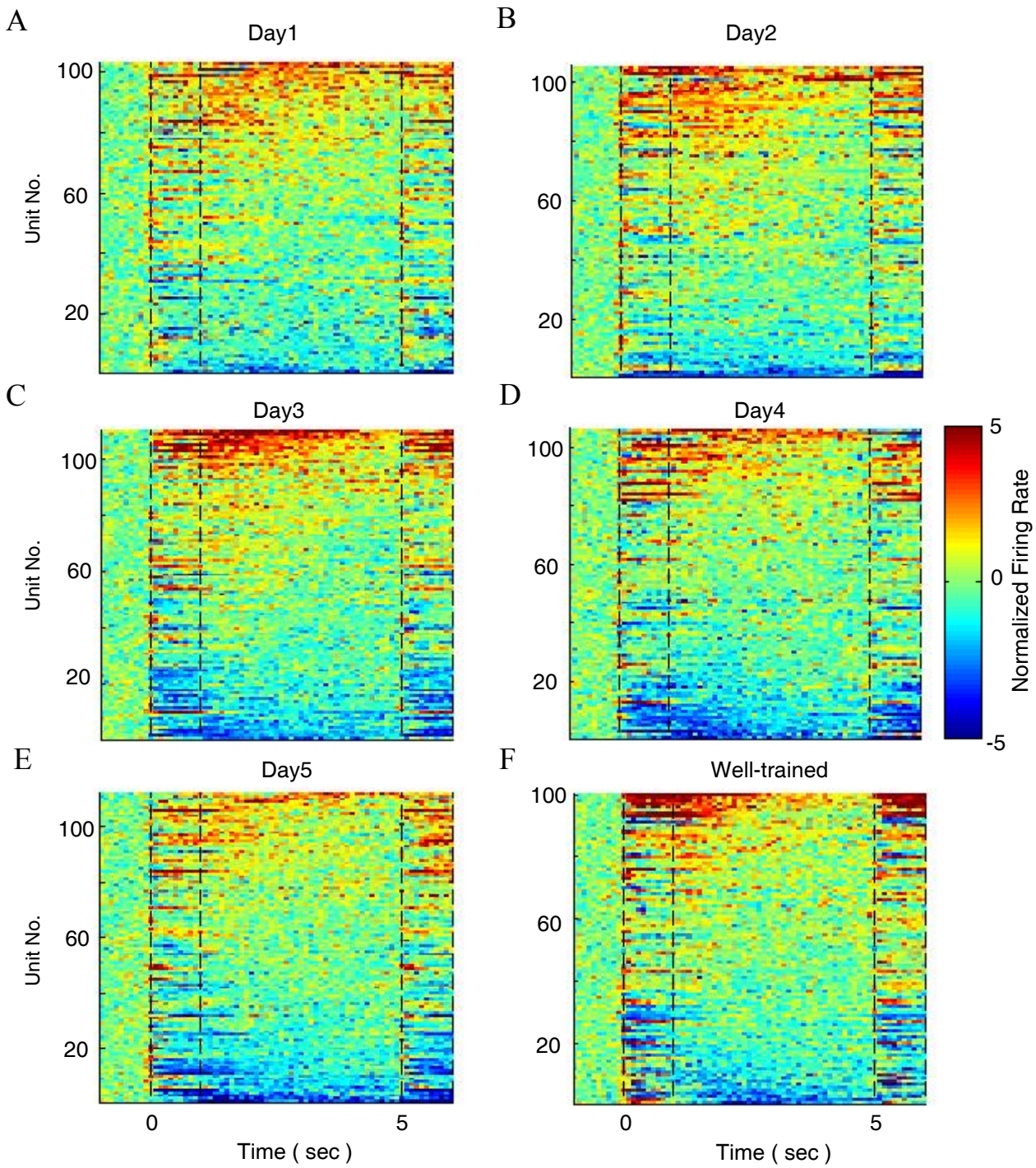

Fig. S26. Firing rate modulation of all neurons recorded with electrodes in fixed locations. (A-F) Each row represented firing rate of one neuron, which was averaged across all trials then normalized in Z-scores. Different panels represented results from Day 1~5 in learning phase and after mice were well-trained (Day 8~10). Number of neurons for each panel: Day1, n=103; Day2, n=105; Day3, n=110; Day4, n=106; Day5, n=112; Well-trained, n=100.

Fig. S27

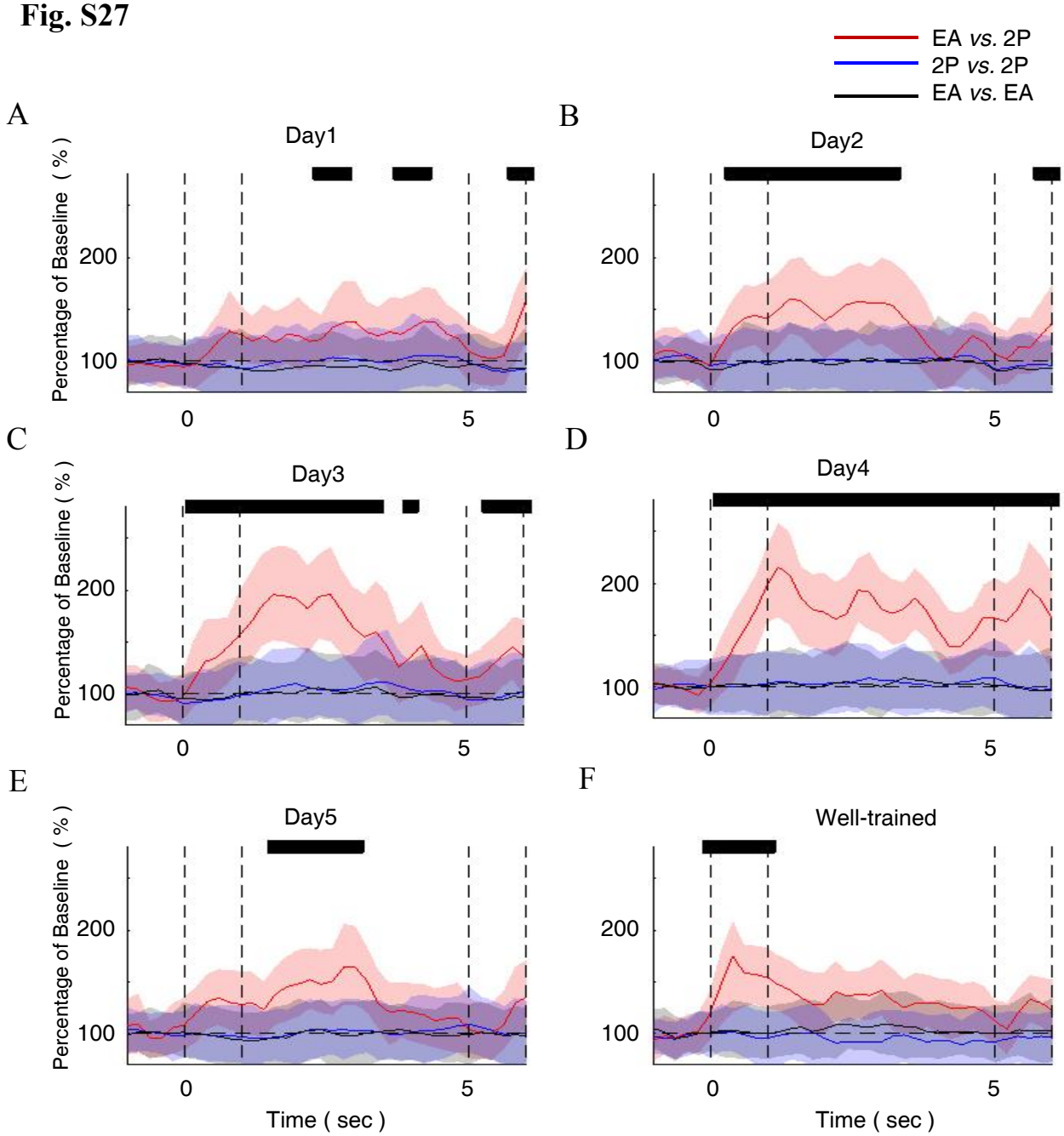

Fig. S27. Progressive modulation in population trajectories in PCA space throughout learning of the WM task, for neurons recorded with electrodes in fixed locations. (A-F) The distances were calculated from the first 20 PCs explaining 80% of variance. Red curves were the distances between different odorants. Black and blue curves were the distances for randomly sampled trials within same odor samples. Black dots: the distances between different odorants were significantly different from the distance within same odorant ($p < 0.05$, Mann-Whitney U-test). Shadow: 95% confidence interval (CI) from bootstrap.

Fig. S28

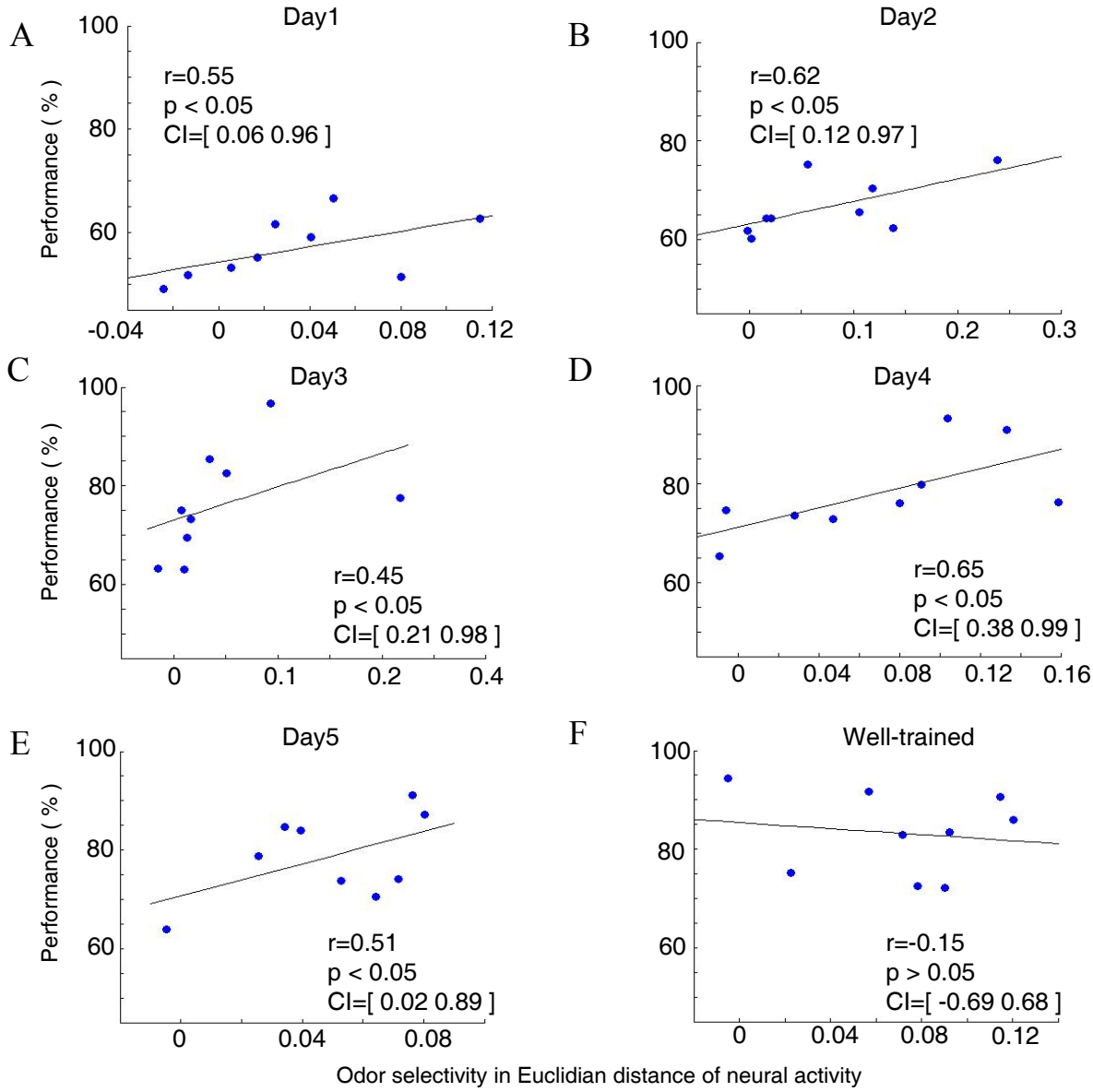

Fig. S28. Correlation between performance and odor selectivity, for neurons recorded with electrodes in fixed locations. (A-F) Correlation was measured by Euclidian distance of neural response following different odor samples, each dot represented performance and averaged odor selectivity for one mouse. Correlation coefficients and 95% confidence intervals of the correlation were marked on figures. Statistics: 95% confidence interval (CI) from bootstrap.

Fig. S29

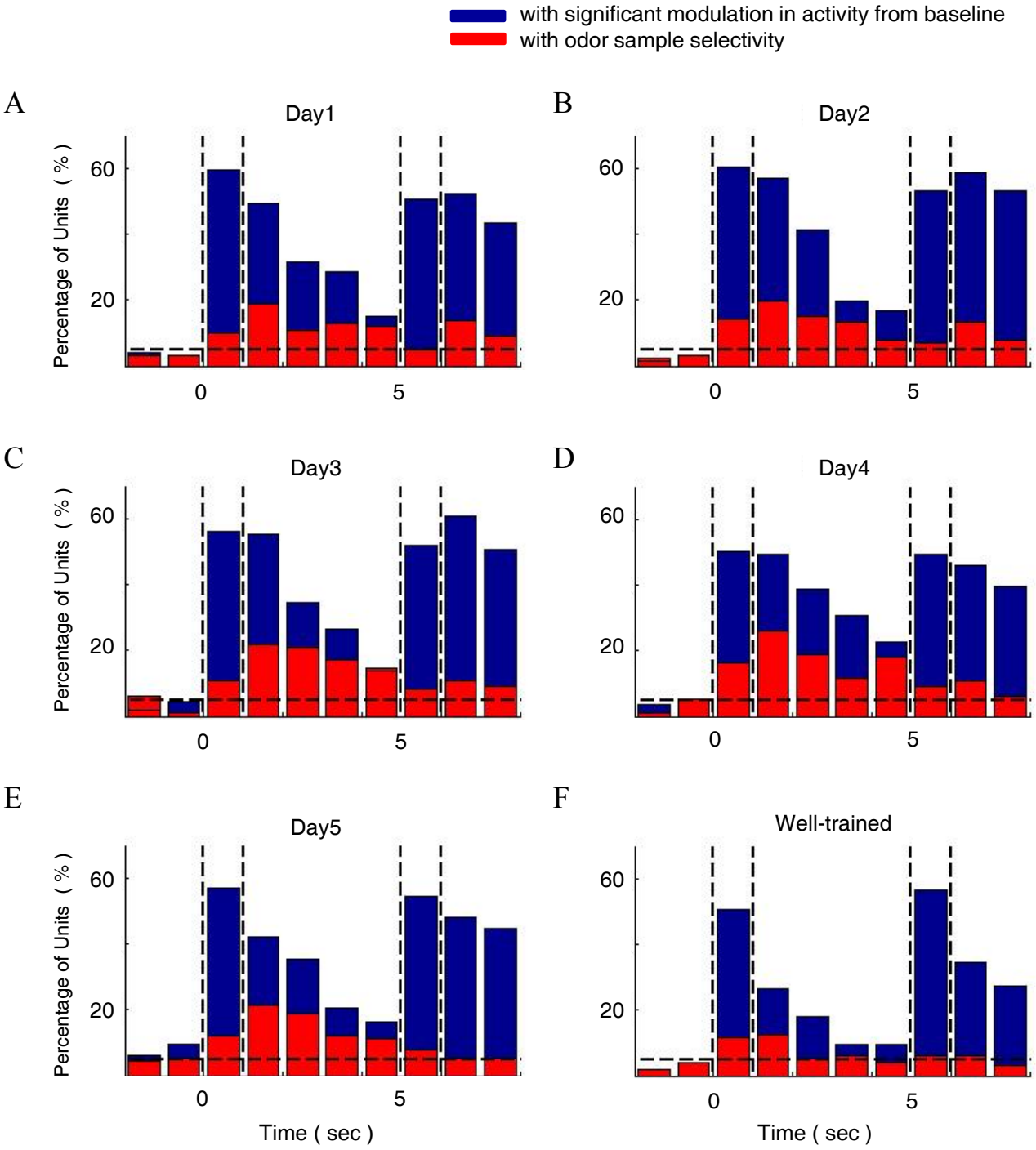

Fig. S29. Percentage of neurons with significant modulation in activity from baseline and odor selectivity in learning and well-trained phases. (A-E) Percentage of neurons exhibited significantly modulated activity (Blue) and odor sample selectivity (Red) in learning phase (Day 1-5). **(F)** As in A-E but in well-trained phase. (Number of neurons: day1: n=101; day2: n=126; day3: n=110; day4: n=111; day5: n=116; well-trained: n=95)

Fig. S30

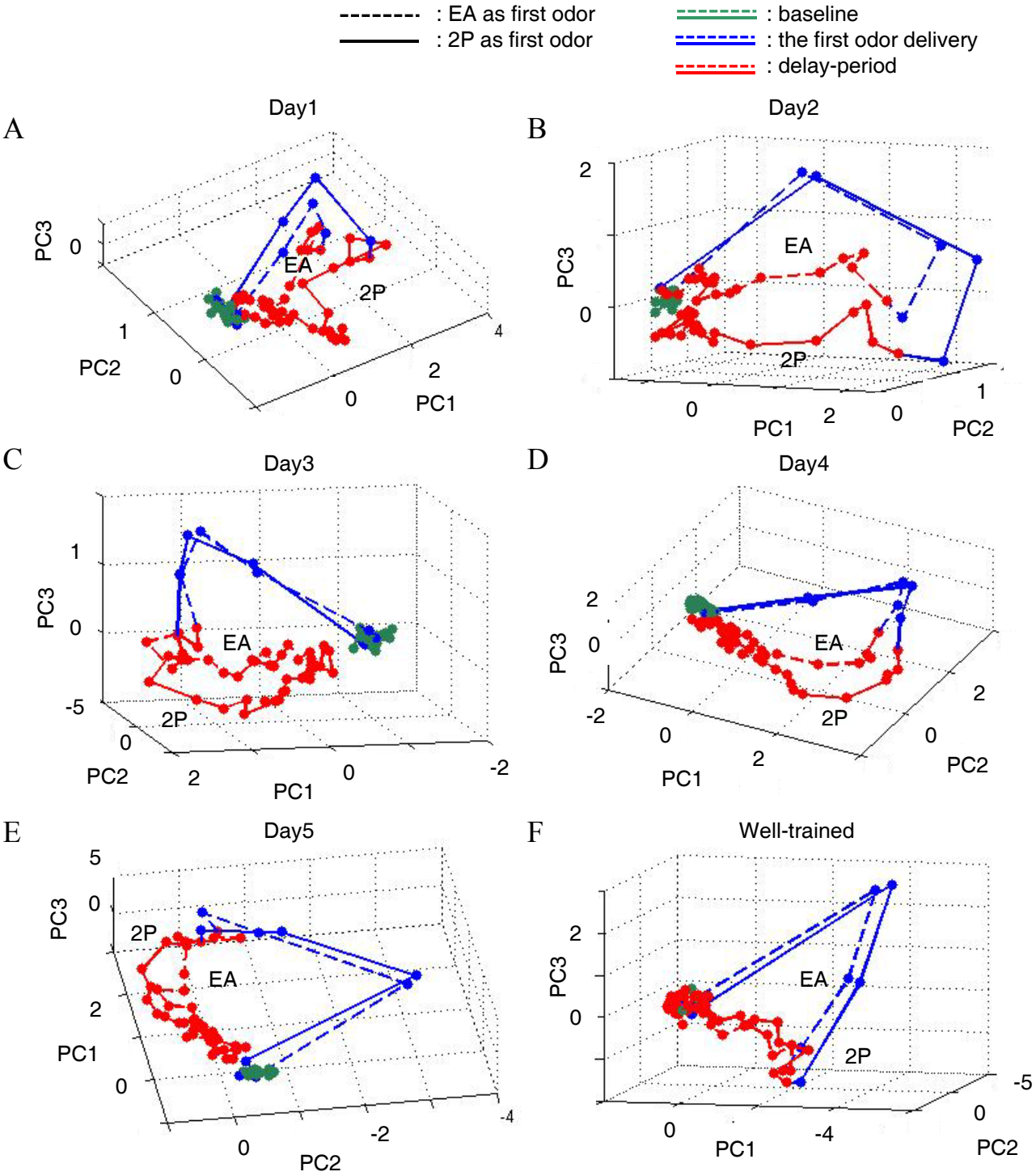

Fig. S30. Example PCA trajectories of trials with EA and 2P as the first odor in learning and well-trained phases of WM task. (A-E) Learning phase (Day 1-5). **(F)** Well-trained phase.

Fig. S31

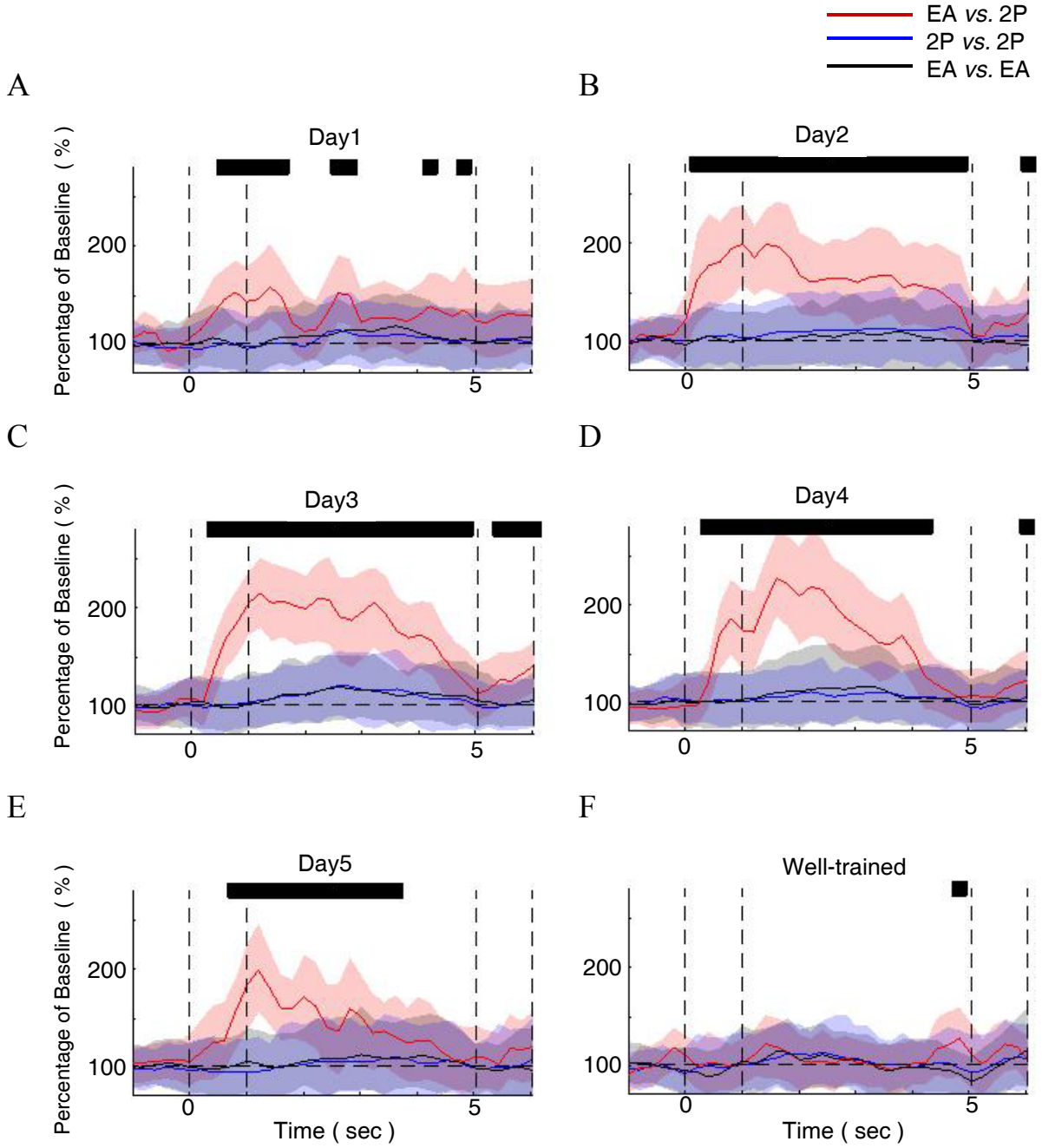

Fig. S31. Greater distance of PCA trajectories in learning phase, calculated with half of neurons recorded. (A-E) In learning (Day 1-5) phase. Bin size: 200 ms. **(F)** In well-trained phase. In each time of PCA calculation, 45 neurons were randomly selected. Averaged PCA distance of 100 times resampling were plotted. Shadow: 95% confidence interval. Black bars on top: bins with mean distance significantly different from baseline, $p < 0.05$, from 95% confidence interval.

Fig. S32

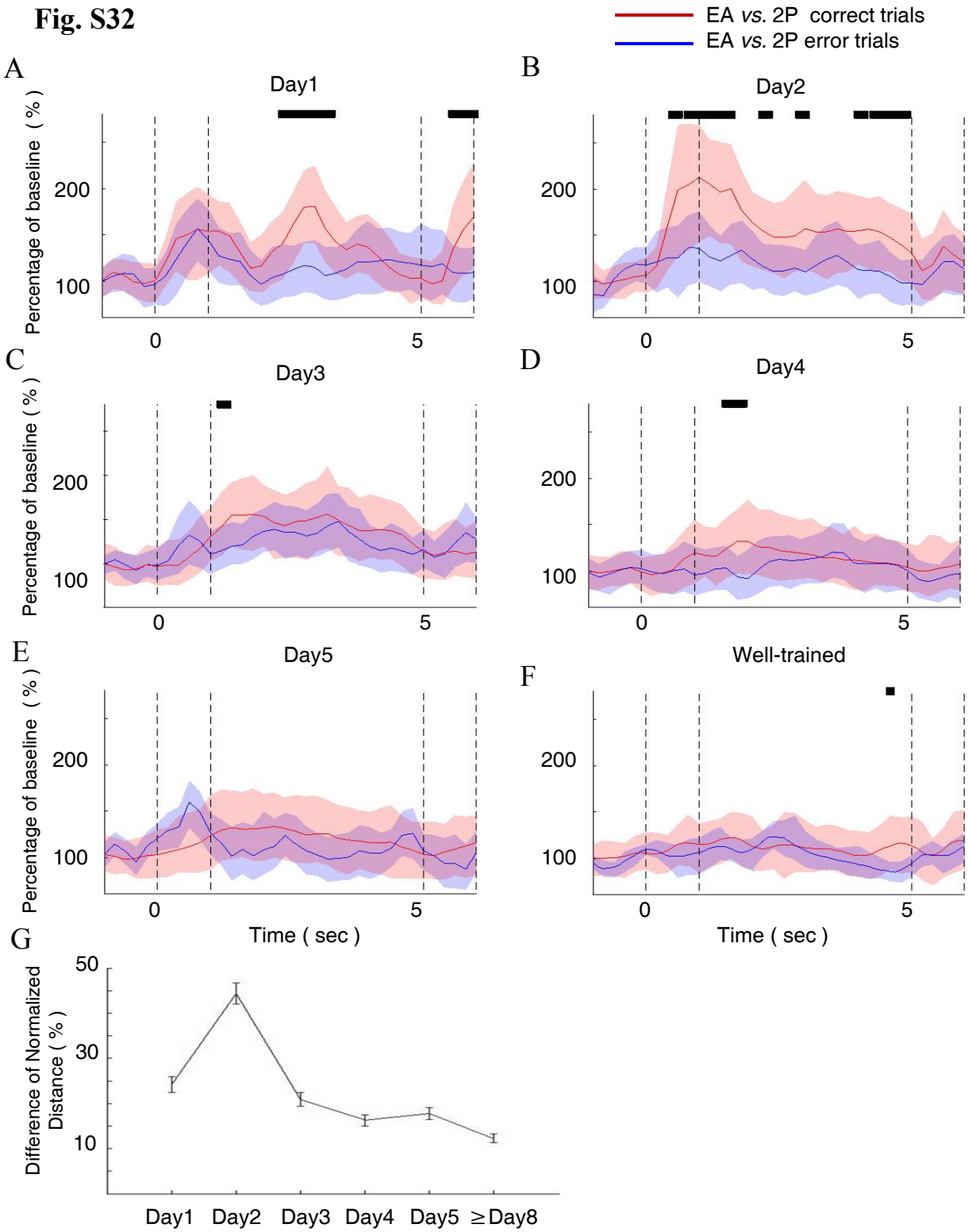

Fig. S32. Population trajectory distance following distinct odor samples were correlated with behavioral performance, during the learning phase but not after mice were well trained. (A-F) The learning related modification in the distance of population trajectories followed by different odor samples, split according to correct and error trials. Black dots: the distances between different odor samples of correct (hit and correct rejection) trials were significantly different from that of error (miss and false choice) trials ($p<0.05$, Mann-Whitney U-test). The number of trials used to analyzing: Day 1, 30 trials; Day 2, 30 trials; Day 3, 20 trials; Day 4, 10 trials; Day 5, 10 trials; Well-trained, 10 trials. **(G)** The averaged difference of PCA trajectories distance during the delay period between different odor samples in correct trials and wrong trials. $p < 0.0001$, ANOVA test for learning related modification.

Fig. S33

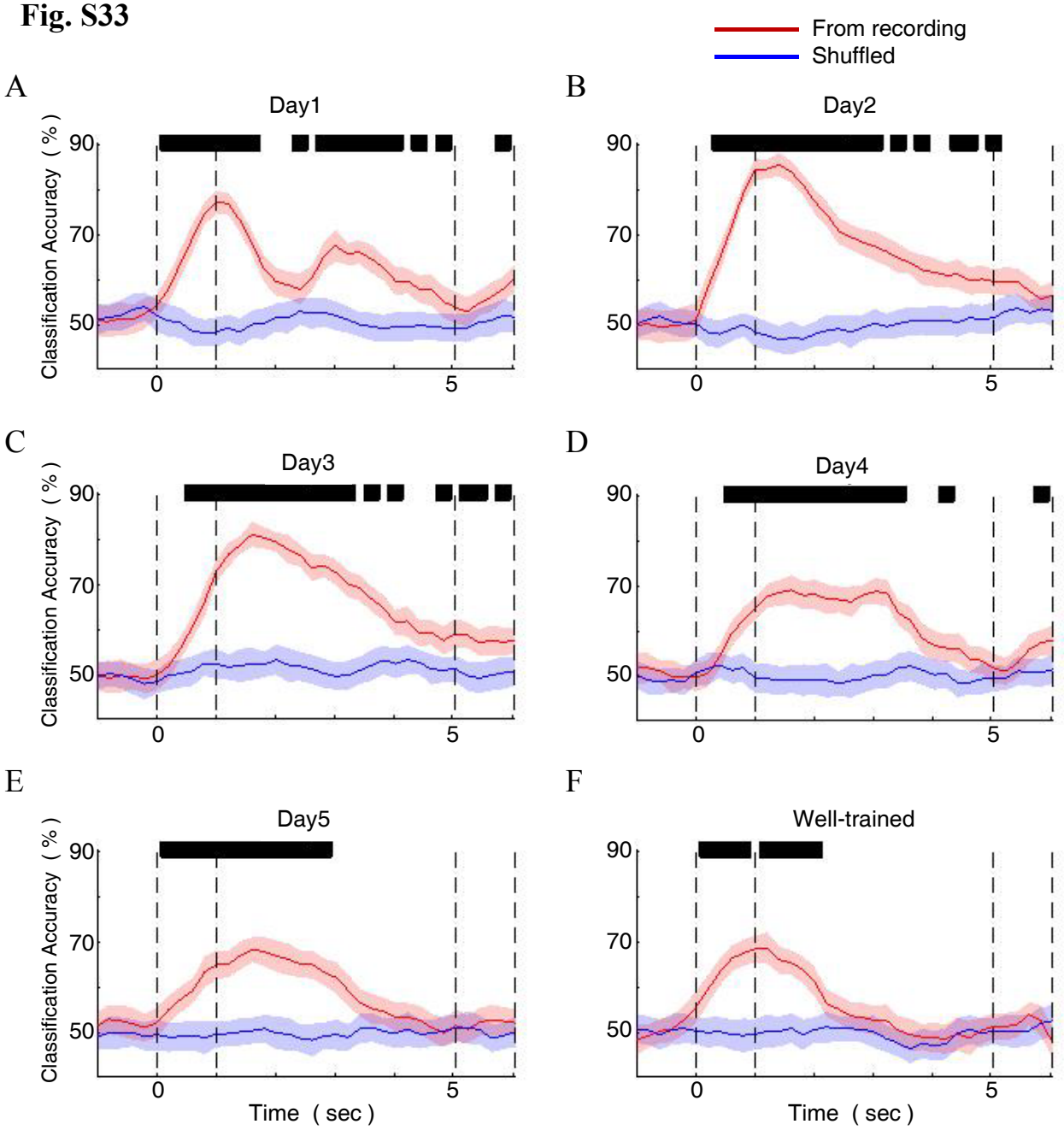

Fig. S33. Delay-period activity during the learning phase exhibited higher decoding power than that in well-trained phase. Classification accuracy of decoding for EA or 2P as the first olfactory input in the learning phase (Day 1-5, **A-E**) and in well-trained phase **(F).** In each time of decoding calculation, 90 neurons were randomly selected. Averaged decoding accuracy of 250 times of resampling were plotted. Shadow: SEM. Black dots on top: bins with mean distance significantly different from baseline, $p < 0.05$, Mann-Whitney U-test.

Fig. S34

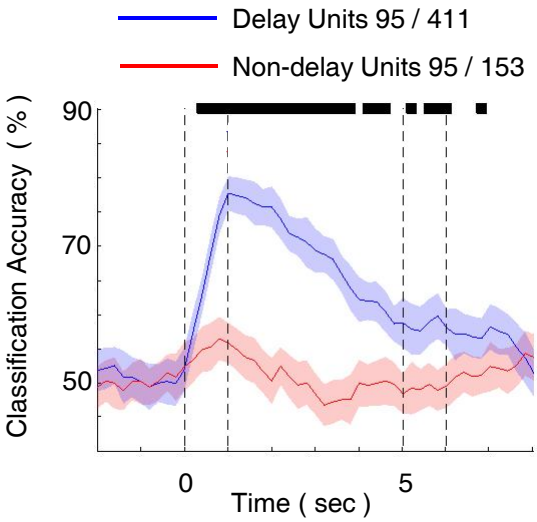

Fig. S34. Higher decoding power by the neurons with significantly modulated delay-period activity than the neurons without. Neurons with or without significantly modulated delay-period activity were classified by Mann-Whitney U-test from baseline activity, using $p < 0.05$ as criterion. In each time of decoding calculation, 90 neurons were randomly selected. Averaged decoding accuracy of 250 times of resampling were plotted. Shadow: SEM. Black bars on top: bins with mean distance significantly different from baseline, $p < 0.05$, Mann-Whitney U-test.

Fig. S35

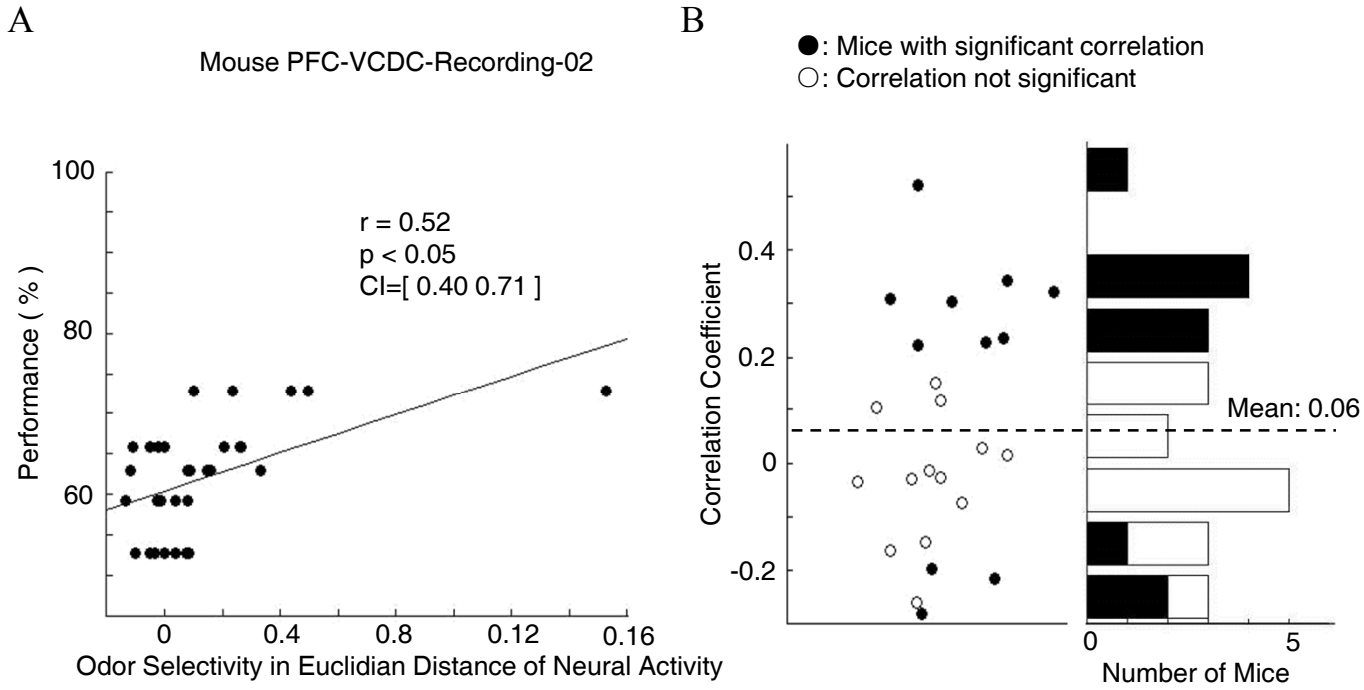

Fig. S35. Correlation between performance and odor selectivity at individual-neuron level. (A) An example illustrating the calculation of correlation coefficient between performance of a mouse in different days and odor selectivity for individual neurons recorded from the mouse. Each dot represented one neuron from the mouse. **(B)** Distribution of correlation coefficient between performance and odor selectivity at individual-neuron level. Each dot represented an individual mouse. Black bars were the distribution of the correlation from 24 mice. The distribution did not have a significant different median from zero (p=0.24, Wilcoxon signed-rank test). Results were obtained from 15 mice with daily lowering of electrodes and 9 mice without.

Tables S1-S8

Table S1.

Data source	**Statistic method**	**Statistic results**	**Mice number**
Performance correct rate in acquisition, hM4D + 1mg/kg CNO *vs* C57+1mg/kg CNO (Fig1. E)	Two-way mixed design ANOVA	$F_{hM4D(1.17)}$=11.84; P_{hM4D}=0.003; $F_{day(4,68)}$=15.379; P_{day}=5.25×10^{-9}; $F_{interaction(4,68)}$=2.69; $P_{interaction}$=0.038;	hM4D+1mg/kg CNO=10 C57+1mg/kg CNO = 9;
Performance correct rate in acquisition, hM4D +1mg/kg CNO *vs* hM4D + saline (Fig1. E)	Two-way mixed design ANOVA	$F_{CNO(1,17)}$=22.89; P_{CNO}=1.72×10^{-4}; $F_{day(4,68)}$=25.38; P_{day}=6.92×10^{-13}; $F_{interaction(4,68)}$=0.88; $P_{interaction}$=0.48;	hM4D+1mg/kg CNO=10; hM4D + saline =9

Statistical results on behavioral performance of DDREAD experiment for DNMS task. Two control groups of wild type mice + CNO and wild type mice + AAV-hM4Di + saline were compared with an experimental group of wild type mice + AAV-hM4Di + CNO. All analyses were based on blind experimental design unless stated otherwise.

Table S2.

Data source	**Statistic method**	**Statistic results**	**Mice number**
Performance correct rate in acquisition, DIO-ChR2 *vs* DIO-mCherry (Fig2. A)	Two-way mixed design ANOVA (use day-based averaged data)	$F_{ChR2(1,18)}$=14.5; P_{ChR2}=0.001; $F_{day(4,72)}$=19.43; P_{day}=7.03×10^{-11}; $F_{interaction(4,72)}$=1.05; $P_{interaction}$=0.39;	ChR2 =10; mCherry=10
Performance correct rate in well train, DIO-ChR2 *vs* DIO-mCherry (Fig2. A)	Mann-Whitney U-test (use day-based averaged data)	P=0.21	ChR2 =10; mCherry=10
Hit rate in acquisition, DIO-ChR2 *vs* DIO-mCherry (Fig2. B left panel)	Two-way mixed design ANOVA	$F_{ChR2(1,18)}$=0.53; P_{ChR2}=0.48; $F_{day(4,72)}$=1.61; P_{day}=0.18; $F_{interaction(4,72)}$=2.17; $P_{interaction}$=0.08;	ChR2 =10; mCherry=10
Hit rate in well train, DIO-ChR2 *vs* DIO-mCherry (Fig2. B left panel)	Mann-Whitney U-test	P=0.75	ChR2 =10; mCherry=10
Correct rejection rate in acquisition, DIO-ChR2 *vs* DIO-mCherry (Fig2. B right panel)	Two-way mixed design ANOVA	$F_{ChR2(1,18)}$=16.03; P_{ChR2}=0.001; $F_{day(4,72)}$=15.66; P_{day}=2.9×10^{-9}; $F_{interaction(4,72)}$=2.59; $P_{interaction}$=0.04;	ChR2 =10; mCherry=10
Correct rejection rate in well train, DIO-ChR2 *vs* DIO-mCherry (Fig2. B right panel)	Mann-Whitney U-test	P=0.11	ChR2 =10; mCherry=10

Statistical results on behavioral performance of suppressing delay-period activities of mPFC pyramidal neurons by enhancing activities of inhibitory neurons with ChR2 in DNMS task. Performance, hit and correct rejection rates were compared between VGAT-Cre mice injected with AAV-DIO-ChR2 and AAV-DIO-mCherry in a blind design. Learning and well-trained phases were separately analyzed.

Table S3.

Data source	**Statistic method**	**Statistic results**	**Mice number**
Performance correct rate in acquisition, NpHR *vs* YFP (Fig2. C)	Two-way mixed design ANOVA (use day-based averaged data)	$F_{eNpHR3.0(1,18)}$=48.99; $P_{eNpHR3.0}$=1.55×10^{-6}; $F_{day(4,72)}$=44.91; P_{day}=7.3×10^{-19}; $F_{interaction(4,72)}$=1.42; $P_{interaction}$=0.24;	NpHR=10; YFP=10
Performance correct rate in well train, NpHR *vs* YFP (Fig2. C)	Mann-Whitney U-test (use day-based averaged data)	P=0.12	NpHR=9; YFP=10
Hit rate in acquisition, NpHR *vs* YFP (Fig2. D left panel)	Two-way mixed design ANOVA	$F_{eNpHR3.0(1,18)}$=0.07; $P_{eNpHR3.0}$=0.79; $F_{day(4,72)}$=0.72; P_{day}=0.58; $F_{interaction(4,72)}$=1.57; $P_{interaction}$=0.19;	NpHR=10; YFP=10
Hit rate in well train, NpHR *vs* YFP (Fig2. D left panel)	Mann-Whitney U-test	P=0.95	NpHR=9; YFP=10
Correct rejection rate in acquisition, NpHR *vs* YFP (Fig2. D right panel)	Two-way mixed design ANOVA	$F_{eNpHR3.0(1,18)}$=57.18; $P_{eNpHR3.0}$=5.42×10^{-7}; $F_{day(4,72)}$=40.71; P_{day}=8.52×10^{-18}; $F_{interaction(4,72)}$=2.4; $P_{interaction}$=0.06;	NpHR=10; YFP=10
Correct rejection rate in well train, NpHR *vs* YFP (Fig2. D right panel)	Mann-Whitney U-test	P=0.48	NpHR=9; YFP=10

Statistical results on behavioral performance of directly suppressing delay-period activities of mPFC pyramidal neurons with NpHR in DNMS task. Performance, hit and correct rejection rates were compared between wild type mice injected with AAV-CaMKIIα-eNpHR3.0 and AAV-CaMKIIα-eYFP in a blind design. Learning and well-trained phases were separately analyzed.

Table S4.

Data source	**Statistic method**	**Statistic results**	**Mice number**
Performance correct rate in acquisition, laser ON *vs* OFF (Fig2. E)	Two-way mixed design ANOVA	$F_{laser(1,9)}$=15.94; P_{laser}=0.003; $F_{day(4,36)}$=18.09; P_{day}=3.17×10^{-8}; $F_{interaction(4,36)}$=0.71; $P_{interaction}$=0.59;	VGAT+ ChR2=10
Hit rate in acquisition, laser ON *vs* OFF (Fig2. F left panel)	Two-way mixed design ANOVA	$F_{laser(1,9)}$=0.62; P_{laser}=0.45; $F_{day(4,36)}$=3.03; P_{day}=0.03; $F_{interaction(4,36)}$=0.16; $P_{interaction}$=0.96;	VGAT+ ChR2=10
Correct rejection rate in acquisition, laser ON *vs* OFF (Fig2. F right panel)	Two-way mixed design ANOVA	$F_{laser(1,9)}$=8.81; P_{laser}=0.016; $F_{day(4,36)}$=13.59; P_{day}=7.5×10^{-7}; $F_{interaction(4,36)}$=0.88; $P_{interaction}$=0.48;	VGAT+ ChR2=10

Statistical results on behavioral performance of suppressing delay-period activities of mPFC pyramidal neurons in DNMS task in an interleaved laser-on and -off manner. Performance, hit and correct rejection rates were compared between laser-on and -off trials for VGAT-Cre mice injected with AAV-DIO-ChR2. Not in blind design.

Table S5.

Data source	**Statistic method**	**Statistic results**	**Mice number**
Performance correct rate in acquisition, ChR2 *vs* mCherry (Fig3. A)	Two-way mixed design ANOVA (use day-based averaged data)	$F_{virus(1,22)}$=12.924; P_{virus} =0.002 $F_{day(4,88)}$=8.951 ; P_{day}=4.1×10^{-6}; $F_{interaction(4,88)}$=0.644; $P_{interaction}$=0.632;	ChR2=12 mCherry=12
Performance correct rate in well train, ChR2 *vs* mCherry (Fig3. A)	Two-way mixed design ANOVA (use session-based data)	$F_{virus(1,22)}$=2.589 ; P_{virus} =0.122 $F_{session(4,88)}$=1.728; $P_{session}$=0.151; $F_{interaction(4,88)}$=0.278; $P_{interaction}$=0.891;	ChR2=12 mCherry=12
Hit rate in acquisition, ChR2 *vs* mCherry (Fig3. B left panel)	Two-way mixed design ANOVA	$F_{virus(1,22)}$=17.364; P_{virus}=4.3×10^{-24} $F_{day(4,88)}$=5.847; P_{day}=0.001; $F_{interaction(4,88)}$=6.584; $P_{interaction}$=0.001;	ChR2=12 mCherry=12
Hit rate in well train, ChR2 *vs* mCherry (Fig3. B left panel)	Mann-Whitney U-test	P=0.838	ChR2=12 mCherry=12
Correct rejection rate in acquisition, ChR2 *vs* mCherry (Fig3. B right panel)	Two-way mixed design ANOVA	$F_{virus(1,22)}$=0.833; P_{virus}=7.4×10^{-23} $F_{day(4,88)}$=4.353 P_{day}=0.028; $F_{interaction(4,88)}$=5.223; $P_{interaction}$=0.001;	ChR2=12 mCherry=12
Correct rejection rate in well train, ChR2 *vs* mCherry (Fig3. B right panel)	Mann-Whitney U-test	P=0.0048	ChR2=12 mCherry=12

Statistical results on behavioral performance of enhancing delay-period activities of mPFC pyramidal neurons in DNMS. Performance, hit, and correct rejection rates were compared between wild type mice injected with AAV-CaMKIIα-ChR2 and AAV-CaMKIIα-mCherry.

Table S6.

Data source	**Statistic method**	**Statistic results**	**Mice number**
Performance correct rate, ChR2 *vs* mCherry (Fig3. C)	Two-way mixed design ANOVA	$F_{virus(1,17)}$=0.11; P_{virus}=0.744; $F_{day(4,68)}$=83.374; P_{day}=1.763×10^{-25}; $F_{interaction(4,68)}$=0.91; $P_{interaction}$=0.463;	ChR2=10 mCherry=9
Hit rate, ChR2 *vs* mCherry (Fig3. D)	Two-way mixed design ANOVA	$F_{virus(1,17)}$=0.647; P_{virus}=0.432; $F_{day(4,68)}$=1.996; P_{day}=0.105; $F_{interaction(4,68)}$=0.192; $P_{interaction}$=0.942;	ChR2=10 mCherry=9
Correct rejection rate, ChR2 *vs* mCherry (Fig3. D)	Two-way mixed design ANOVA	$F_{virus(1,17)}$=0.788; P_{virus}=0.387; $F_{day(4,68)}$=59.757; P_{day}=1.514×10^{-21}; $F_{interaction(4,68)}$=0.812; $P_{interaction}$=0.522;	ChR2=10 mCherry=9

Statistical results on behavioral performance of suppressing activities of mPFC pyramidal neurons in NMS-WD. Laser-on period covered sensory perception, decision making, and motor selection. Performance, hit, and, correct rejection rates were compared between results from VGAT-Cre mice injected with AAV-DIO-ChR2 and those with AAV-DIO-mCherry.

Table S7.

Data source	**Statistic method**	**Statistic results**	**Mice number**
Performance correct rate, ChR2 *vs* mCherry (Fig3. E)	Two-way mixed design ANOVA	$F_{virus(1,18)}$=0.055; P_{virus}=0.817; $F_{session(7,126)}$=62.593; $P_{session}$=5.276×10^{-38}; $F_{interaction(7,126)}$=0.629; $P_{interaction}$=0.732;	ChR2=10 mCherry=10
Hit rate, ChR2 *vs* mCherry (Fig3. F)	Two-way mixed design ANOVA	$F_{virus(1,18)}$=0.239; P_{virus}=0.631; $F_{session(7,126)}$=0.802; $P_{session}$=0.587; $F_{interaction(7,126)}$=0.312; $P_{interaction}$=0.948;	ChR2=10 mCherry=10
Correct rejection rate, ChR2 *vs* mCherry (Fig3. F)	Two-way mixed design ANOVA	$F_{virus(1,18)}$=0.369; P_{virus}=0.551; $F_{session(7,126)}$=47.192; $P_{session}$=2.818×10^{-32}; $F_{interaction(7,126)}$=0.474; $P_{interaction}$=0.852;	ChR2=10 mCherry=10

Statistical results on behavioral performance of suppressing activities of mPFC pyramidal neurons in GNG task. Laser-on period was preceding sensory perception period to simulate laser illumination in experiment of Fig. 2A-2D. To make this period task-relevant, we have added a trial-starting cue 5 sec before the onset of Go/No-go cue and randomized the inter-trial interval (in 6-10 sec range). Performance, hit and correct rejection rates were compared between results from VGAT-Cre mice injected with AAV-DIO-ChR2 and those with AAV-DIO-mCherry.

Table S8.

Data source	**Analyzed period**	**Statistic method**	**Statistic results**	**Neuron number**
Average firing rate of neurons with enhanced delay-period activities, learning phase *vs* well-trained phase (Fig4. E)	Early 2s of delay	Mann-Whitney U-test test	P=0.45	Learning phase:311 Well-trained phase:48
	Later 2s of delay	Mann-Whitney U-test test	$P=3.5\times10^{-6}$	Learning phase:311 Well-trained phase:48
Average firing rate of neurons with suppressed delay-period activities, learning phase *vs* well-trained phase (Fig4. E)	Early 2s of delay	Mann-Whitney U-test test	$P=3.5\times10^{-5}$	Learning phase:253 Well-trained phase:47
	Later 2s of delay	Mann-Whitney U-test	P=0.95	Learning phase:253 Well-trained phase:47

Statistical results on modulation of delay-period activities of mPFC neurons in learning and well-trained phases of DNMS task. Averaged firing rates of neurons with enhanced or suppressed delay-period activities were separately analyzed. Delay-period was separated into early and late delay-period, in which the trend of difference in modulation was qualitatively different for enhanced and suppressed neurons.

Captions for Movies S1 and S2

Mov. S1. Example of behavioral performance from a well-trained mouse in the WM task. The first trial was a non-match trial with hit response. The turning-on of the first LED indicated for the odor delivery of odorant EA (ethyl acetate), whereas the second LED for delivery of 2P (2-pentanone). The interval between the turning-on of these two LEDs was the delay period. The turning-on of the third LED indicated for the opening of water-delivery valve. The second trial in movie was a match trial with response of correct rejection, in which LED indicated for EA in both odor deliveries. In normal training, mice cannot perceive visual inputs from these LEDs.

Mov. S2. Population dynamics of neural responses to odor samples as revealed by PCA trajectories. Each dot represented for population projection onto the first three PCs for a given time bin (size: 200 ms). The solid and dashed lines indicated for trials with odor sample of EA and 2P, respectively. Green, blue, and red curves represented results from the baseline, odor sample, and delay period. Videos were played at the real time. Note the separation of two trajectories in the delay period for Day 2 in learning but not for well-trained phase, which was further revealed by rotation of PC coordinate frame in 3D.

References and Notes

1. A. D. Baddeley, *Working Memory* (Oxford Univ. Press, Oxford, 1986).

2. E. K. Miller, J. D. Cohen, An integrative theory of prefrontal cortex function. *Annu. Rev. Neurosci.* **24**, 167–202 (2001). Medline doi:10.1146/annurev.neuro.24.1.167

3. J. M. Fuster, *The Prefrontal Cortex* (Academic Press, London, ed. 4, 2008).

4. J. M. Fuster, G. E. Alexander, Neuron activity related to short-term memory. *Science* **173**, 652–654 (1971). Medline doi:10.1126/science.173.3997.652

5. E. K. Miller, C. A. Erickson, R. Desimone, Neural mechanisms of visual working memory in prefrontal cortex of the macaque. *J. Neurosci.* **16**, 5154–5167 (1996). Medline

6. R. Romo, C. D. Brody, A. Hernández, L. Lemus, Neuronal correlates of parametric working memory in the prefrontal cortex. *Nature* **399**, 470–473 (1999). Medline doi:10.1038/20939

7. E. H. Baeg, Y. B. Kim, K. Huh, I. Mook-Jung, H. T. Kim, M. W. Jung, Dynamics of population code for working memory in the prefrontal cortex. *Neuron* **40**, 177–188 (2003). Medline doi:10.1016/S0896-6273(03)00597-X

8. S. Fujisawa, A. Amarasingham, M. T. Harrison, G. Buzsáki, Behavior-dependent short-term assembly dynamics in the medial prefrontal cortex. *Nat. Neurosci.* **11**, 823–833 (2008). Medline doi:10.1038/nn.2134

9. J. C. Erlich, M. Bialek, C. D. Brody, A cortical substrate for memory-guided orienting in the rat. *Neuron* **72**, 330–343 (2011). Medline doi:10.1016/j.neuron.2011.07.010

10. E. M. Meyers, X. L. Qi, C. Constantinidis, Incorporation of new information into prefrontal cortical activity after learning working memory tasks. *Proc. Natl. Acad. Sci. U.S.A.* **109**, 4651–4656 (2012). Medline doi:10.1073/pnas.1201022109

11. R. Desimone, Neural mechanisms for visual memory and their role in attention. *Proc. Natl. Acad. Sci. U.S.A.* **93**, 13494–13499 (1996). Medline doi:10.1073/pnas.93.24.13494

12. R. E. Passingham, S. P. Wise, *The Neurobiology of the Prefrontal Cortex: Anatomy, Evolution, and the Origin of Insight* (Oxford Univ. Press, Oxford, ed. 1, 2012).

13. S. H. Wang, R. G. Morris, Hippocampal-neocortical interactions in memory formation, consolidation, and reconsolidation. *Annu. Rev. Psychol.* **61**, 49–79, C1–C4 (2010). Medline doi:10.1146/annurev.psych.093008.100523

14. R. Dias, J. P. Aggleton, Effects of selective excitotoxic prefrontal lesions on acquisition of nonmatching- and matching-to-place in the T-maze in the rat: Differential involvement of the prelimbic-infralimbic and anterior cingulate

cortices in providing behavioural flexibility. *Eur. J. Neurosci.* **12**, 4457–4466 (2000). Medline doi:10.1046/j.0953-816X.2000.01323.x

15. D. R. Euston, A. J. Gruber, B. L. McNaughton, The role of medial prefrontal cortex in memory and decision making. *Neuron* **76**, 1057–1070 (2012). Medline doi:10.1016/j.neuron.2012.12.002

16. K. Matsumoto, W. Suzuki, K. Tanaka, Neuronal correlates of goal-based motor selection in the prefrontal cortex. *Science* **301**, 229–232 (2003). Medline doi:10.1126/science.1084204

17. E. A. Allen, B. N. Pasley, T. Duong, R. D. Freeman, Transcranial magnetic stimulation elicits coupled neural and hemodynamic consequences. *Science* **317**, 1918–1921 (2007). Medline doi:10.1126/science.1146426

18. S. Sobotka, M. D. Diltz, J. L. Ringo, Can delay-period activity explain working memory? *J. Neurophysiol.* **93**, 128–136 (2005). Medline doi:10.1152/jn.01002.2003

19. T. Otto, H. Eichenbaum, Neuronal activity in the hippocampus during delayed non-match to sample performance in rats: Evidence for hippocampal processing in recognition memory. *Hippocampus* **2**, 323–334 (1992). Medline doi:10.1002/hipo.450020310

20. X.-C. M. Lu, B. M. Slotnick, A. M. Silberberg, Odor matching and odor memory in the rat. *Physiol. Behav.* **53**, 795–804 (1993). Medline doi:10.1016/0031-9384(93)90191-H

21. L. Fenno, O. Yizhar, K. Deisseroth, The development and application of optogenetics. *Annu. Rev. Neurosci.* **34**, 389–412 (2011). Medline doi:10.1146/annurev-neuro-061010-113817

22. B. N. Armbruster, X. Li, M. H. Pausch, S. Herlitze, B. L. Roth, Evolving the lock to fit the key to create a family of G protein-coupled receptors potently activated by an inert ligand. *Proc. Natl. Acad. Sci. U.S.A.* **104**, 5163–5168 (2007). Medline doi:10.1073/pnas.0700293104

23. H. T. Chao, H. Chen, R. C. Samaco, M. Xue, M. Chahrour, J. Yoo, J. L. Neul, S. Gong, H. C. Lu, N. Heintz, M. Ekker, J. L. Rubenstein, J. L. Noebels, C. Rosenmund, H. Y. Zoghbi, Dysfunction in GABA signalling mediates autism-like stereotypies and Rett syndrome phenotypes. *Nature* **468**, 263–269 (2010). Medline doi:10.1038/nature09582

24. S. B. Ostlund, B. W. Balleine, Lesions of medial prefrontal cortex disrupt the acquisition but not the expression of goal-directed learning. *J. Neurosci.* **25**, 7763–7770 (2005). Medline doi:10.1523/JNEUROSCI.1921-05.2005

25. M. Rabinovich, R. Huerta, G. Laurent, Neuroscience. Transient dynamics for neural processing. *Science* **321**, 48–50 (2008). Medline doi:10.1126/science.1155564

26. E. M. Meyers, D. J. Freedman, G. Kreiman, E. K. Miller, T. Poggio, Dynamic population coding of category information in inferior temporal and prefrontal cortex. *J. Neurophysiol.* **100**, 1407–1419 (2008). Medline doi:10.1152/jn.90248.2008

27. M. Stopfer, G. Laurent, Short-term memory in olfactory network dynamics. *Nature* **402**, 664–668 (1999). Medline doi:10.1038/45244

28. C. D. Harvey, P. Coen, D. W. Tank, Choice-specific sequences in parietal cortex during a virtual-navigation decision task. *Nature* **484**, 62–68 (2012). Medline doi:10.1038/nature10918

29. Z. V. Guo, N. Li, D. Huber, E. Ophir, D. Gutnisky, J. T. Ting, G. Feng, K. Svoboda, Flow of cortical activity underlying a tactile decision in mice. *Neuron* **81**, 179–194 (2014). Medline doi:10.1016/j.neuron.2013.10.020

30. J. Yamamoto, J. Suh, D. Takeuchi, S. Tonegawa, Successful execution of working memory linked to synchronized high-frequency gamma oscillations. *Cell* **157**, 845–857 (2014). Medline doi:10.1016/j.cell.2014.04.009

31. N. Uchida, Z. F. Mainen, Speed and accuracy of olfactory discrimination in the rat. *Nat. Neurosci.* **6**, 1224–1229 (2003). Medline doi:10.1038/nn1142

32. B. Slotnick, A simple 2-transistor touch or lick detector circuit. *J. Exp. Anal. Behav.* **91**, 253–255 (2009). Medline doi:10.1901/jeab.2009.91-253

33. N. A. Macmillan, C. D. Creelman, *Detection Theory: A User's Guide* (Lawrence Erlbaum, Mahwah, NJ, ed. 2, 2005).

34. C. M. Niell, M. P. Stryker, Modulation of visual responses by behavioral state in mouse visual cortex. *Neuron* **65**, 472–479 (2010). Medline doi:10.1016/j.neuron.2010.01.033

35. B. L. McNaughton, J. O'Keefe, C. A. Barnes, The stereotrode: A new technique for simultaneous isolation of several single units in the central nervous system from multiple unit records. *J. Neurosci. Methods* **8**, 391–397 (1983). Medline doi:10.1016/0165-0270(83)90097-3

36. M. A. Wilson, B. L. McNaughton, Dynamics of the hippocampal ensemble code for space. *Science* **261**, 1055–1058 (1993). Medline doi:10.1126/science.8351520

37. G. Buzsáki, Large-scale recording of neuronal ensembles. *Nat. Neurosci.* **7**, 446–451 (2004). Medline doi:10.1038/nn1233

38. L. Lin, G. Chen, K. Xie, K. A. Zaia, S. Zhang, J. Z. Tsien, Large-scale neural ensemble recording in the brains of freely behaving mice. *J. Neurosci. Methods* **155**, 28–38 (2006). Medline doi:10.1016/j.jneumeth.2005.12.032

39. D. P. Nguyen, S. P. Layton, G. Hale, S. N. Gomperts, T. J. Davidson, F. Kloosterman, M. A. Wilson, Micro-drive array for chronic in vivo recording: Tetrode assembly. *J. Vis. Exp.* **2009**, 1098 (2009). Medline

40. M. S. Fee, P. P. Mitra, D. Kleinfeld, Automatic sorting of multiple unit neuronal signals in the presence of anisotropic and non-Gaussian variability. *J. Neurosci. Methods* **69**, 175–188 (1996). Medline doi:10.1016/S0165-0270(96)00050-7

41. L. Hazan, M. Zugaro, G. Buzsáki, Klusters, NeuroScope, NDManager: A free software suite for neurophysiological data processing and visualization. *J. Neurosci. Methods* **155**, 207–216 (2006). Medline doi:10.1016/j.jneumeth.2006.01.017

42. J. K. Chapin, M. A. Nicolelis, Principal component analysis of neuronal ensemble activity reveals multidimensional somatosensory representations. *J. Neurosci. Methods* **94**, 121–140 (1999). Medline doi:10.1016/S0165-0270(99)00130-2